University of Crete

Department of Physics

Master thesis

Intense femtosecond photoexcitation of bulk and monolayer MoS_2

Ioannis M. Paradisanos

Supervisor: Prof. Costas Fotakis

Co-supervisors: Dr. Emmanuel Stratakis

Prof. George Kioseoglou

September 2014

CONTENTS

ACKNOWLEDGEMENTS

My special and heartily thanks to my principal supervisor, Professor Costas Fotakis. This thesis would not have been possible without his encouragement, motivation, enthousiasm and support. He taught me how to question thoughts and express ideas.

I would like to express my deepest gratitude to my second supervisor Dr. Emmanuel Stratakis, for his excellent guidance, caring and providing me with an excellent atmosphere for doing research. He has supported me throughout my thesis with his knowledge and patience whilst allowing me the room to work in my own way. I attribute the level of my Masters degree to his encouragement and effort and without him this thesis, would not have been completed or written. I have been amazingly fortunate to have an advisor like him. He gave me the freedom to explore on my own, and at the same time the guidance to recover when my steps faltered. He really knows how to keep my performance in the highest level possible.

I owe my sincere gratitude to my special advisor, Professor George Kioseoglou, who has been always there to listen and give advice. I am deeply grateful to him for the long discussions that helped me sort out the theoretical and technical details of my work. Our countless conversations analyzing the physical mechanisms that explain experimental results related to our field of research, always raised my interest and made my days really enjoyable. I really hope that the "team: Stratakis-Kioseoglou-Paradisanos" will always work and cooperate together as one, because this makes me dream of the future.

I am so grateful to the Institute of Electronic Structure and Laser (IESL) of the Foundation for Research and Technology-Hellas (FORTH) for the financial support, equipment and for making it possible for me to do research and study here.

I want to express my thankfulness to Dr. Emmanouel Spanakis for his patience, knowledge and for his significant advices. He has always been willing to help me and carry out the AFM measurements.

On a more personal level, I must thank my patient and understanding girlfriend Stevy and I want to express my love and gratitude for her invaluable support.

I would also like to thank my parents. They were always supporting me and encouraging me with their best wishes.

A final thanks goes to my friends, George Ktistakis and Giannis Flouris, who supported me and influenced me along the way.

ABSTRACT

Molybdenum disulfide (MoS_2) is a two-dimensional inorganic compound classified as a metal dichalcogenide. It is a 2D-semiconductor that has attracted great interest because of its distinctive electronic, optical, and catalytic properties, as well as its importance for dry lubrication. Its physical properties make it desirable for various optoelectronic and photonic applications, including phototransistors, light emitters, and heterojunction solar cells. Towards the development of 2D photonic devices, the investigation of 2D materials response under intense photoexcitation by ultrashort pulses, as well as of their ultrafast optical properties, including nonlinear susceptibility, refraction, absorption, and carrier relaxation, is undoubtedly important.

In this thesis, the intense femtosecond laser excitation on the structure of bulk and monolayer MoS_2, under conditions ranging from lattice heating to material damage is experimentally investigated. For this purpose, the intensity of A_{1g} and E^1_{2g} vibrational modes was recorded as a function of the number of irradiation pulses. Through this process, the single-pulse damage threshold in monolayer MoS_2 was identified and compared to that of the bulk crystal. Besides this, optical and field emission scanning electron microscopy (FESEM) were used for the optical damage quantification. Experiments reveal large differences in the ultrafast laser excitation response of monolayer compared to the bulk.

FIGURES

PREAMBLE

Atomically thin two-dimensional (2D) materials including graphene have attracted in the latest years significant research interest due to their extraordinary physical properties[1,2]. Graphene has been theoretically studied as early as 1947 but was thought to be unstable at room temperature because of thermal fluctuations. More than 60 years later and after a Nobel prize, graphene is undoubtedly one of the most intensively researched materials and has been selected as one of the flagship research projects that will lead Europe's research in the next ten years. All around the globe, dedicated graphene research centres open while companies such as IBM and many more also study the possible use of graphene's outstanding properties and explore ways to engineer them. However, graphene is a zero band gap material which in some cases is an undesirable property for optoelectronic applications[3]. Transition metal dichalcogenides (TMDs) combine the 2D layered structure with a finite band gap and therefore are considered to be alternatives of graphene[4]. Among TMDs, Molybdenum disulfide (MoS_2) is one of the most stable ones and it is widely known as one of the most common solid lubricants. In bulk form it is an indirect band gap semiconductor with an energy gap, E_g of 1.3 eV. Upon reducing the number of layers, MoS_2 undergoes a transition from an indirect to a direct band gap semiconductor reaching an optical gap of 1.9 eV in monolayer form[2,5-7].

Apart from its direct bandgap, monolayer MoS_2 exhibits a stable charge exciton state even at room temperature, a property that is desirable for various optoelectronic and photonic applications[8], including phototransistors[9,10], light emitters[11], and heterojunction solar cells[12,13]. Towards the development of 2D photonic devices, the investigation of 2D materials response under intense photoexcitation by ultrashort pulses, as well as of their ultrafast optical properties, including nonlinear susceptibility, refraction, absorption, and carrier relaxation, is undoubtedly important. For example, recent investigations have focused on the nonlinear optical properties of monolayer MoS_2[14] paving the way for applications including mode-lock devices, laser protection optical limiters, saturable absorbers, and optical switches.

Another aspect of the intense photoexcitation properties of monolayer MoS_2 is the evolution of the structure during heating, melting/resolidification, and finally optical damage. Although, a previous work has shown that continuous wave (CW) laser irradiation can be employed for photo-thermal thinning of bulk MoS_2 crystals down to monolayer[15], to date

there is no investigation of the MoS_2 lattice response under ultrashort pulsed laser photoexcitation conditions. A unique characteristic of ultrashort (i.e., sub-picosecond) laser-material interaction is that the photon energy is transferred to the lattice at rates faster than the electron-phonon relaxation time. Such ultrafast absorption process could give rise to both thermal and non-thermal effects within the lattice. In addition to this, the study of the monolayer response compared to that of the bulk is of great interest. This thesis is a modest contribution to the study of the fundamental differences in optical absorption properties of direct compared to indirect gap semiconductors. The work is organized as follows.

In part I and specifically in chapter 1, the production methods, the structural, electronic, optical and mechanical properties of MoS_2 crystal are presented. A theoretical approach of single and two-photon absorption, as well as optical damage is discussed in chapter 2. In addition, theoretical aspects of Raman spectroscopy and specifically the Raman spectrum of MoS_2 are explained in the same chapter. Furthermore, a brief reference of the experimental methods, as well as the instrumentation used in this work, is demonstrated in chapter 3.

The experimental results of this thesis are presented in part II. The effect of intense femtosecond laser excitation on the structure of bulk and monolayer MoS_2, under conditions ranging from lattice heating to material damage is systematically investigated. Optical, field emission scanning electron microscopy (FESEM) and Raman microscopy were used to quantify the damage. In particular, the intensity of A_{1g} and E^1_{2g} vibrational modes was recorded as a function of the number of irradiation pulses. Additionally, the single-pulse damage threshold in monolayer MoS_2 was identified and compared to that of the bulk crystal. Experiments reveal large differences in the ultrafast laser excitation response of monolayer compared to the bulk, as far as the lattice distortion as well as the lattice morphology, at the onset of optical damage. These differences are understood as the result of a two-photon absorption process versus single-photon absorption for these two different systems.

In part III, future work and perspectives are presented. A challenging target is to try to isolate a single layer of GeSe, a very promising 2D crystal with (estimated) unusual optical, mechanical, and electronic properties in its monolayer form and these properties remain unknown by the scientific community until now. Furthermore, Raman spectroscopy was introduced to examine the response of the two prominent Raman modes of bulk GeSe, under different values of laser intensity. The results appear very intriguing and need further investigation.

Part I:
Introduction

CHAPTER 1

MOLYBDENUM DISULFIDE

1.1 Bulk and atomically thin MoS_2 production methods

In nature, molybdenum occurs primarily as molybdenite, a mineral that occurs in high temperature hydrothermal ore deposits and is similar in appearance and feel to graphite. Molybdenite is processed by flotation to give relatively pure Molybdenum disulfide (MoS_2), the main contaminant being carbon. It also arises by the thermal treatment of virtually all molybdenum compounds with hydrogen sulfide or elemental sulfur. Another way of production is by metathesis reactions from molybdenum pentachloride[16].

Single layer MoS_2 can be isolated by the micromechanical exfoliation of bulk molybdenum disulfide crystal. This, so-called "scotch-tape" method, was first introduced by K.S. Novoselov et al., for the isolation of graphene from natural graphite[17]. A natural, bulk piece of MoS_2 is peeled several times between two pieces of an adhesive tape and the resulting mixture of thick and thin flakes is deposited on a Si/Silicon Oxide wafer for an optimum contrast that eases the optical detection of ultrathin flakes of MoS_2. This method is widely used in the research community as it allows the production of single, bi or triple layers from a bulk crystal piece with a very low defect concentration. However, its poor yield and the relatively small sizes of the flakes (about 1-5μm) are the two main disadvantages of the micromechanical exfoliation method.

Joensen et al. exfoliated MoS_2 into monolayers by intercalation with lithium followed by a reaction with water. Chemically exfoliated MoS_2 was also prepared via lithium intercalation using a solution of butyllithium in hexane[18]. However, this method resulted in loss of semiconducting properties of the pristine MoS_2, due to the structural changes that occurred

during Li intercalation[19]. Rao and Nag described the preparation of MoS_2 sheets by lithium intercalation followed by exfoliation of the layers by ultrasonication and chemical synthesis, where molybdic acid was treated with an excess of thiourea[20].

Chemical vapor deposition (CVD) has been one of the most practical methods for synthesizing large-area graphene[21]. CVD is also adopted to synthesize MoS_2 layer directly on SiO_2/Si substrates using MoO_3 and S powders as the reactants. The growth of MoS_2 is very sensitive to the substrate treatment prior to the growth. The use of graphene-like molecules for the substrate treatment, such as reduced graphene oxide (rGO), perylene-3,4,9,10-tetracarboxylic acid tetrapotassium salt (PTAS) and perylene-3,4,9,10-tetracarboxylic dianhydride (PTCDA), promotes the layer growth of MoS_2[22]. Besides the combination of MoO_3 and S powders as precursors, pre-deposited Mo film can also be used to react with sulfur vapor[23]. Although this approach can facilitate the large-area synthesis of MoS_2 films over a length scale of a few inches, it can be difficult to control the number of layers and the uniformity of the layer distribution. Residual Mo atoms tend not to react and remain with the sulfur atoms. Another CVD method presents the development of a large-area synthesis for preparing high-quality MoS_2 films using H_2S gas and a Mo metal source. This approach offers important advantages over other CVD methods, including (i) uniform layer thicknesses over a large substrate area, such as SiO_2 or quartz, up to the wafer scale and (ii) readily controllable film thickness by changing the thickness of the deposited metal source[24].

Finally, a top-down approach to fabricate MoS_2 single layers is laser thinning of multilayered molybdenum disulfide using a scanning laser from a confocal Raman microscope to thin the multilayered MoS_2 down to a monolayer by moving the laser over the flake with high power. This provides a reliable method to fabricate MoS_2 single layers with user-defined shape and size and with optical and electronic properties that are comparable to those of pristine MoS_2 single layers[25].

1.2 Crystal Structure

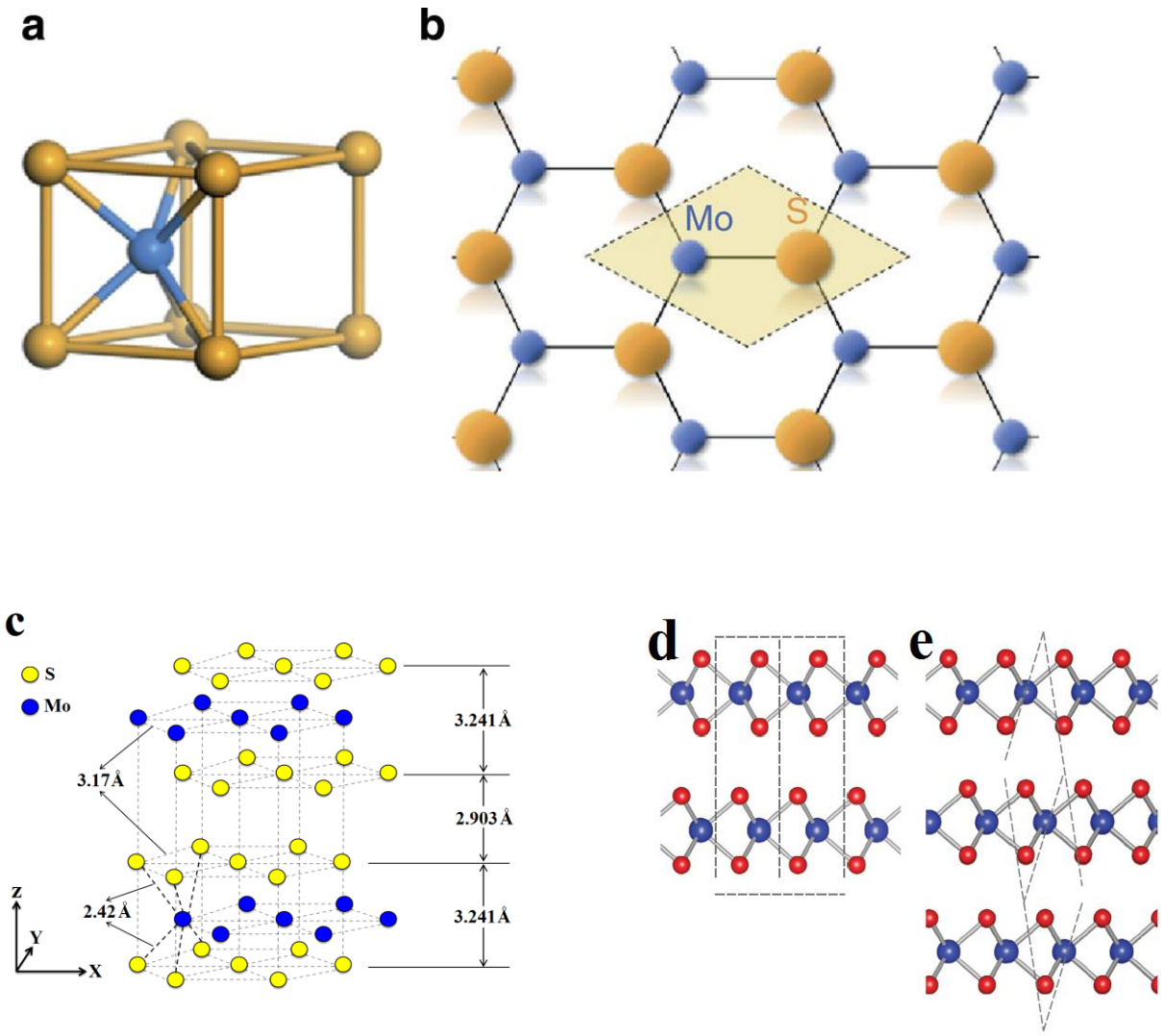

Fig. 1.1: a) Coordination environment of Mo (blue sphere) in the structure. Molybdenum is shown as a blue sphere and Sulphur is shown as golden spheres[26]. b) A top view of the monolayer MoS_2 lattice, emphasizing the connection to a honeycomb lattice[26]. The shaded region bounded by dashed lines corresponds to one primitive cell. c) 2H-type crystal structure of MoS_2. Schematic shows Mo–Mo, S–S, Mo–S bond distances and S–S planar distances[27]. d,e) Side views of two forms of MoS_2: 2H-type crystal (d) and 3R crystal (e). Blue and red spheres correspond to Molybdenum and Sulphur atoms, respectively. Black dashed lines indicate unit cells[28].

The molybdenum disulfide belongs to the large family of layered transition metal dichalcogenides whose crystal structure results from the stacking of sheets of hexagonally packed atoms (Fig. 1.1b). It consists of weakly coupled sandwich layers S-Mo-S in which a

Molybdenum atomic layer is enclosed within two Sulfur atomic layers. The sandwich layers are coupled only by weak van der Waals forces giving rise to the quasi-two dimensional character of the electronic structure. Because of the weak van der Waals interactions between the sheets of sulfide atoms, MoS_2 has a low coefficient of friction, producing its lubricating properties.

Naturally occurring MoS_2 has two polytypes, 2H and 3R, both having the trigonal prismatic coordination (Fig. 1.1a). While the 2H-type (Fig. 1.1c,d) has two layers per unit cell stacked in the hexagonal symmetry, the 3R-type (Fig 1.1e) has three layers per cell in the rhombohedral symmetry. The 2H-type is dominant and more stable in nature, and 3R will transform to 2H upon heating[29]. This is the reason why the 2H will be the main type discussed in this thesis.

1.3 Electronic Structure

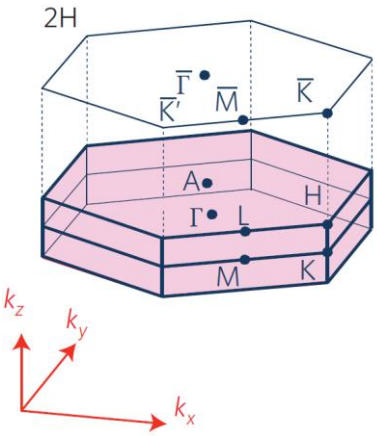

Fig. 1.2: First Brillouin zone of bulk 2H-MoS_2. The hexagonal plane with $\bar{\Gamma}, \bar{M}, \bar{K}, \bar{K}'$, represents the corresponding two dimensional projected Brillouin zone.

The corresponding first Brillouin zone of the hexagonal Bravais lattice of bulk 2H-MoS_2 along with the different crystallographic symmetry directions is shown in figure 1.2. This is a representation of the lattice of molybdenum disulfide in the crystal's reciprocal space and is obtained by Fourier transformation of the Cartesian crystal structure. The Brillouin zone's centre Γ is the origin of the reciprocal space with $k_x = 0$, $k_y=0$ and $k_z=0$. In the table below we show the values of the wave vector momentum k for each symmetry point:

Symmetry point	$[k_x,k_y,k_z]$
Γ	[0,0,0,]
A	[0,0,π/c]
K	[4π/3a,0,0]
H	[4π/3a,0,π/c]
M	[π/a,-π/√3a,0]
L	[π/a,-π/√3a, π/c]

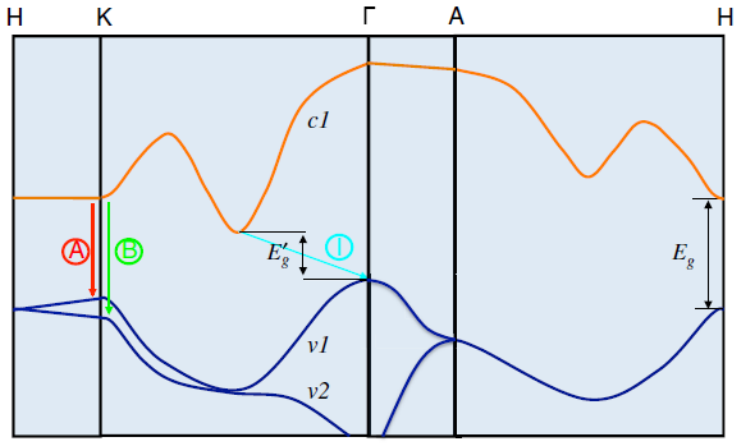

Fig. 1.3: Simplified band structure of bulk MoS_2, showing the lowest conduction band c1 and the highest split valence bands v1 and v2. A and B are the direct-gap transitions, and I is the indirect-gap transition. E'_g is the indirect gap for the bulk, and E_g is the direct gap for the monolayer[2].

The band structure of bulk MoS_2 calculated from first principles show indirect-semiconducting behavior with a bandgap of 1.3 eV, which originates from transition from the top of valence band situated at Γ-point to the bottom of conduction band halfway between Γ and K high symmetry points (Fig. 1.3). As the number of layers decreases, the indirect bandgap increases. In the monolayer, the material changes into a 2D direct bandgap semiconductor with an optical gap of 1.9 eV. At the same time, the optical direct gap (at the K point) stays almost unchanged (independent of layer thickness) and close to the value of the optical direct bandgap (at the K point) of a bulk system (Fig. 1.4)[30].

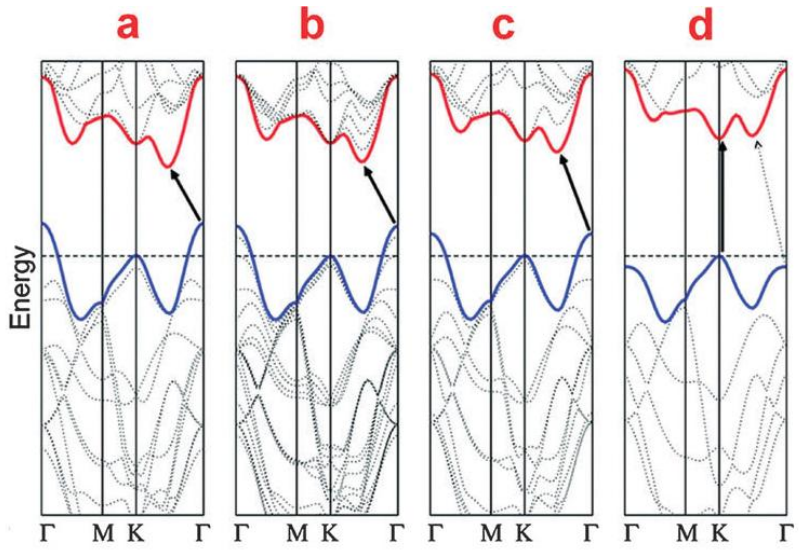

Fig. 1.4: Calculated band structures of (a) bulk MoS_2, (b) quadric-layer MoS_2, (c) bi-layer MoS_2, and (d) monolayer MoS_2. The solid arrows indicate the lowest energy transitions. Bulk MoS_2 is characterized by an indirect bandgap. The direct excitonic transitions occur at high energies at K point. With reduced layer thickness, the indirect bandgap becomes larger, while the direct excitonic transition barely changes. For monolayer MoS_2 (d), it becomes a direct bandgap semiconductor[47].

It is important to mention that the calculated bandgap of MoS_2 monolayer varies from 1.6 to 1.9 eV from the literature due to different approximations for the exchange and correlation functional forms[32-42]. The theoretical results based on the Perdew–Burke–Ernzerhof functional form of the generalized gradient approximation showed that the bandgap of MoS_2 monolayer is about 1.9 eV[32], which agrees with the experimental data observed from photoluminescence[2]. It is known, however, that DFT always underestimates the bandgaps of materials due to the calculated unreliable exited states. Furthermore, the strong exciton binding due to the weak screening compared to bulk cases in low-dimensional systems may affect the bandgap. Therefore, the good bandgap agreement between theoretical and experimental results for MoS_2 monolayer may be a mere coincidence. The GW approximation is expected to calculate more accurate gaps and predicted that the gap of the single layer MoS_2 is 2.7–2.9 eV due to the effect of confinement and environment on the electronic structure and exciton binding energy[42-44]. It was argued that the experimentally observed gap was optical gap and the exciton binding energy was about 0.8–1.0 eV[42-44]. The fundamental bandgap of MoS_2 monolayer, therefore, is about 2.8 eV. The direct experimental confirmation on the prediction is still not available, and the issue is open to question.

The band structure and bandgap of MoS_2 monolayer are very sensitive to the external strain[45,46]. Compared to that of graphene, a much smaller amount of strain is required to vary the bandgap of MoS_2 monolayer. Mechanical strain leads to a reduced bandgap of MoS_2 monolayer causing a direct -to- indirect bandgap transition. In addition, the results

demonstrate that a homogeneous biaxial tensile strain of around 10 % leads to semiconductor-to-metal transition in MoS_2 monolayer (Fig. 1.5)[45].

The band-gap energy of semiconductors tends to decrease with increasing temperature. When temperature increases, so does the amplitude of atomic vibrations, leading to larger interatomic spacing. The interaction between the lattice phonons and the free electrons and holes will also affect the band gap to a smaller extent. The relationship between band gap energy and temperature of a material can be described by Varshni's empirical expression:

$$E_g(T) = E_g(0) - \frac{aT^2}{T+\beta}$$

,where $E_g(0)$ is the value of the band gap energy for T=0K, α is related to electron-phonon interaction and β is related to the Debye temperature.

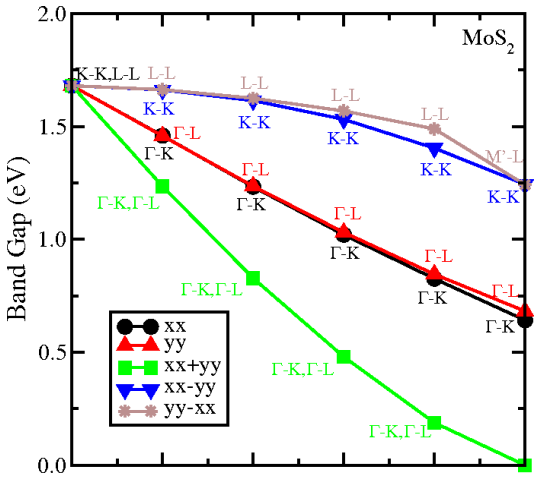

Fig. 1.5: Bandgap of MoS_2 monolayer with respect to strain, ε, which varies from 0 to 10 %. Strain is applied to the optimized structures (ε=0) through various approaches, such as uniaxial expansion in x-direction (xx), y-direction (yy), homogeneous expansion in both x- and y-directions (xx+yy), expansion in x-direction and compression in y-direction (xx-yy), and compression in x-direction and expansion in y direction (yy-xx) with same magnitude of strain. The first three strain profiles correspond to tensile strain, while the latter two represent pure shear strain[45].

1.4 Optical properties

The evolution of electronic structures of MoS_2 nanosheets with various thicknesses can be reflected in their photoluminescence (PL) spectra. As an indirect-gap material, band-gap PL in bulk MoS_2 is a weak phonon-assisted process and is known to show negligible PL intensity. However, appreciable PL is observed from few-layer MoS_2 samples, and surprisingly bright PL, from monolayer samples[2]. The photoluminescence spectrum of suspended monolayer samples consists of a single narrow feature of 50 meV width, centered at 1.90 eV. In contrast, few-layer samples display multiple emission peaks (labeled A, B, and I in Figures 1.3 and 1.6). Peak A coincides with the monolayer emission peak. It shifts to the

red and broadens slightly with increasing the number of layers, N. Peak B lies about 150 meV above peak A. The energy difference between these two peaks arises from the splitting of the valence band energy at the K-point of the Brillouin zone[47]. The inversion symmetry breaking of the material, results in a large spin splitting at the valence band top with opposite spin moments at the two valleys.[48,49]

The broad feature I, which lies below peak A, systematically shifts to lower energies, approaching the indirect-gap energy of 1.29 eV and becomes less prominent with increasing N (Fig. 1.6). This feature is attributed to indirect-gap luminescence[2].

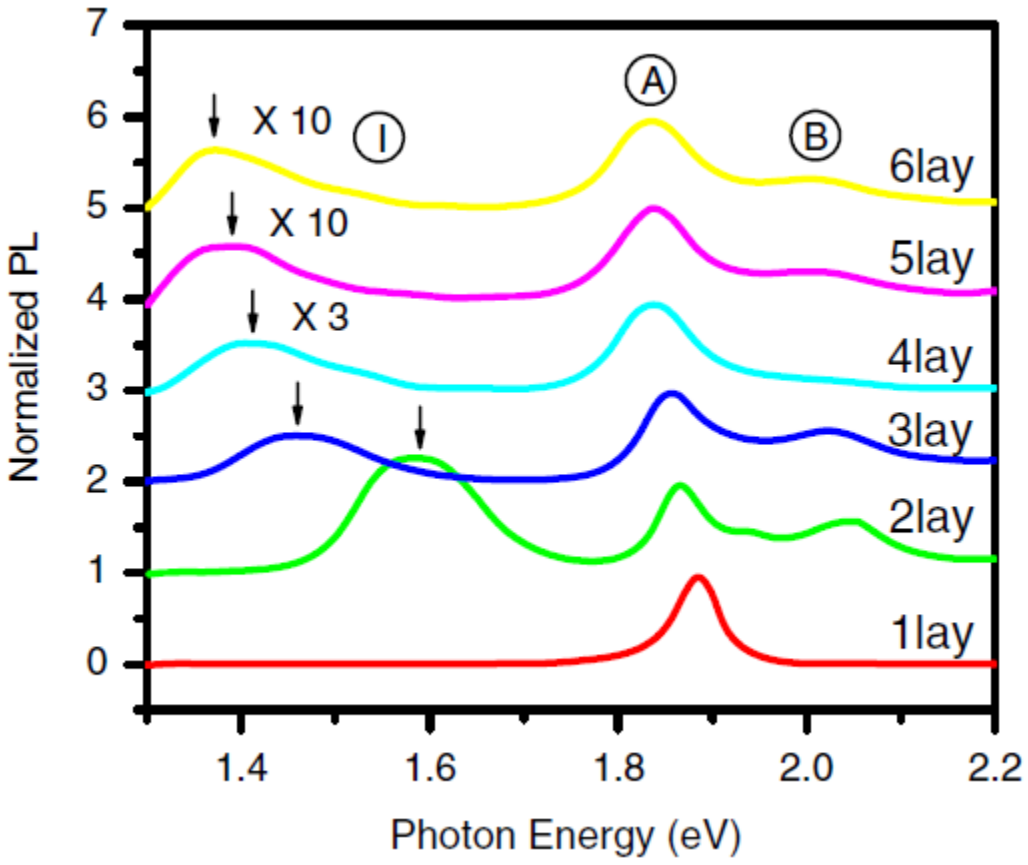

Fig. 1.6: Normalized PL spectra by the intensity of peak A of thin layers of MoS_2 for N=1–6. Feature I for N=4–6 is magnified and the spectra are displaced for clarity[2].

It has been shown by Mak et al, that PL intensity is inversely dependent on the layer number of MoS_2 nanosheets, and the monolayer exhibits the strongest PL intensity and highest quantum efficiency[2] (Fig 1.7).

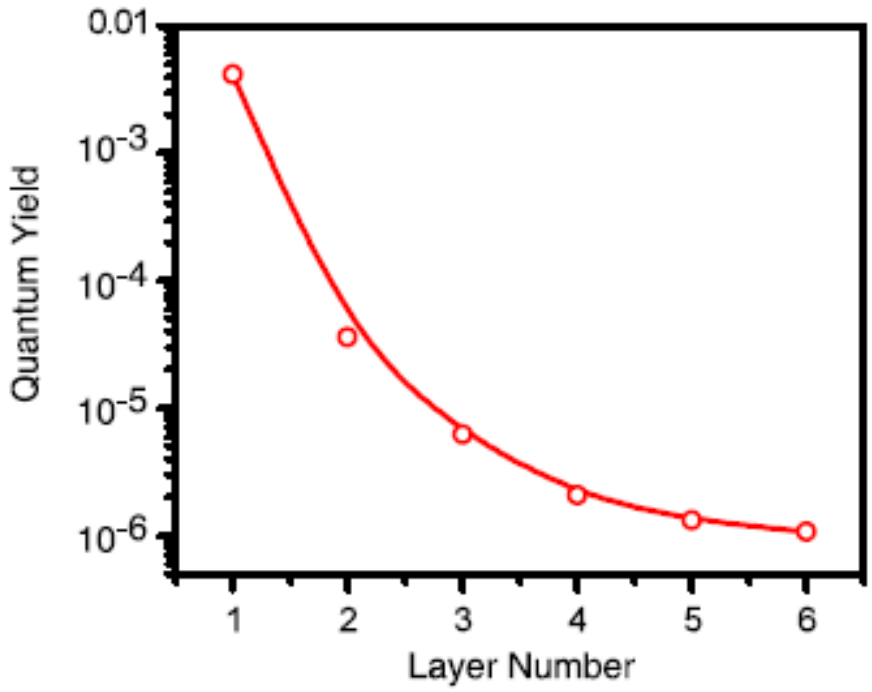

Fig. 1.7: Photoluminescence quantum yield (QY) of thin layers for N=1-6 [2].

Optical absorption is another characteristic which is related to the band structure of a semiconductor. There are usually two absorption peaks observed for thin MoS_2 layers deposited on Si/SiO_2, corresponding to the direct excitonic transitions at the K-point of the Brillouin zone (Fig. 1.8) [2]. However, these absorption peaks exhibit little change with sample thickness.

Fortunately, the contrast of a thin MoS_2 layer deposited on a Si/SiO_2 substrate, which is due to the phase shift of the light interference and variation in material opacity, is directly related to the thickness, reflective index and absorption constant of the MoS_2 and SiO_2 layers[50]. Taking this as an advantage, Benameur et al. were able to distinguish the single-, double- and triple-layer MoS_2 on 90 or 270 nm SiO_2 by measuring the image contrast under green light illumination[50]. However, this method requires filtered light to give the distinguishable image contrast.

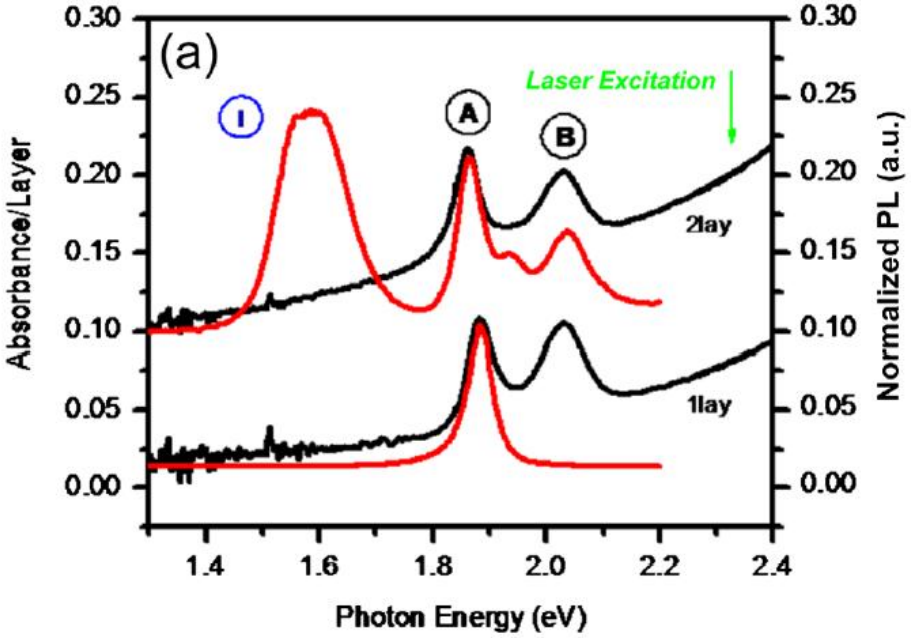

Fig. 1.8: Absorption spectra (left axis, normalized by N) and the corresponding PL spectra (right axis, normalized by the intensity of the peak A). The spectra are displaced along the vertical axis for clarity. The weak feature between A and B for the PL of the bilayer could be impurity or defect luminescence and merits further investigation[2].

1.5 Mechanical properties

Studies of the elastic properties of freely suspended MoS_2 nanosheets, with thicknesses ranging from 5 to 25 layers have shown that the average Young's modulus of the MoS_2 sheets, is exceptionally high, i.e. E = 0.33 ± 0.07 TPa, which is comparable to that of graphene oxide. This value is also higher than the Young's modulus of bulk MoS_2 (i.e. 0.24 TPa), most likely resulting from the lower density of stacking faults present in thinner flakes compared to the bulk crystal. Moreover, these nanosheets exhibited low pre-strain and could stand elastic deformations up to tens of nanometers without breaking. The measurement was performed by using an AFM tip which applied load in the center of the suspended region of a MoS_2 nanosheet. The sheet deformation (δ) was determined by the equation $\delta = \Delta Z_{piezo} - \Delta Z_c$, where ΔZ_{piezo} is the displacement of the AFM scanning piezotube and ΔZ_c is the deflection of an AFM cantilever[51]. Another work showed that the measured Young's modulus of a monolayer MoS_2 was ~0.27 TPa, lower than that of multi-layers but higher than that of the bulk form[52]. These results indicate that monolayer MoS_2 is a flexible and strong material with

a high Young's modulus, comparable to stainless steel. The measured strength of monolayer MoS_2 is close to the theoretical intrinsic strength of the Mo-S chemical bond, indicating that the monolayer is mostly free of defects and dislocations capable of reducing mechanical strength. The exceptional mechanical properties of monolayer MoS_2 make it suitable for incorporation into flexible electronic devices where commonly used substrates such a polyimide (PI) would undergo mechanical failure at a smaller deformation than MoS_2.

CHAPTER 2

THEORY OF TWO-PHOTON ABSORPTION, AND RAMAN SPECTROSCOPY

This chapter introduces a simple theoretical background of two-photon absorption and a brief discussion about optical damage. It also presents the theory of Raman spectroscopy on crystals with a focus on Molybdenum disulfide.

2.1 Two-photon absorption

Nonlinear optics (NLO) is the branch of optics that describes the behavior of light in nonlinear media, that is, media in which the dielectric polarization *P* responds nonlinearly to the electric field *E* of the light. For example, second-harmonic generation occurs as a result of the part of the atomic response that scales quadratically with the strength of the applied optical field. This nonlinearity is typically only observed at very high light intensities such as those provided by lasers.

In order to describe more precisely what we mean by an optical nonlinearity, let us consider how the dipole moment per unit volume, or polarization $\tilde{P}(t)$, of a material system depends on the strength $\tilde{E}(t)$ of an applied optical field. In the case of linear optics, the induced polarization depends linearly on the electric field strength in a manner that can often be described by the relationship:

$$\tilde{P}(t) = \varepsilon_0 \chi^{(1)} \tilde{E}(t) \,, \tag{2.1.1}$$

where the constant of proportionality $\chi^{(1)}$ is known as the linear susceptibility and ε_0 is the permittivity of free space. In nonlinear optics, the optical response can often be described by

generalizing Eq. (2.1.1) by expressing the polarization $\tilde{P}(t)$ as a power series in the field strength $\tilde{E}(t)$ as:

$$\tilde{P}(t) = \varepsilon_0\left[\chi^{(1)}\tilde{E}(t) + \chi^{(2)}\tilde{E}^2(t) + \chi^{(3)}\tilde{E}^3(t) + \ldots\right]$$
$$\equiv \tilde{P}^{(1)}(t) + \tilde{P}^{(2)}(t) + \tilde{P}^{(3)}(t) + \ldots \qquad (2.1.2)$$

The quantities $\chi^{(2)}$ and $\chi^{(3)}$ are known as the second and third order nonlinear optical susceptibilities, respectively. For simplicity, we have taken the fields P(t) and E(t) to be scalar quantities in writing Eqs. (2.1.1) and (2.1.2). In writing Eqs. (2.1.1) and (2.1.2) in the forms shown, we have also assumed that the polarization at time t depends only on the instantaneous value of the electric field strength.

Two-photon absorption (TPA) is a third order nonlinear optical phenomenon in which a material absorbs two photons at the same time. The transition energy for this process is equal to the sum of the energies of the two photons absorbed. The probability that a material undergoes two-photon absorption depends on the square of the intensity of the incident light, if the two photons are from the same beam (in the case of two incident beams, the transition probability depends on the product of the beams intensities). Two-photon absorption in a material can be quantified by the two-photon absorption cross section, a quantity that is proportional to the imaginary component of the $\chi^{(3)}$ tensor and depends on the photon energy/energies. We only discuss the case of degenerate (or one color) two-photon absorption, that is the case where the two photons have the same energy. This is illustrated in the figure 2.1. For most known materials the two-photon absorption cross section, δ, is small and it is necessary to use intense laser beams in order to observe the effects of two-photon absorption. The rate equation that describes the formation of the excited state of a material by one-photon absorption (OPA) can we written as follows:

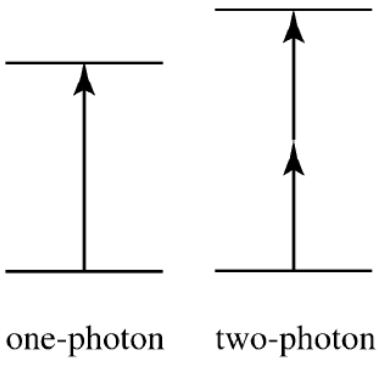

Figure 2.1: Schematic representation of one- and two-photon absorption.

$$\frac{dN_{OP}}{dt} = \sigma N_{GS} F$$

where,

σ, is the one-photon absorption cross section (related to the transition dipole moment of the atom/molecule between the initial and final states of the transition)

N_{GS} , is the number of atoms/molecules per unit volume in the ground state

N_{OP} , is the number of atoms/molecules per unit volume in the excited state due to one-photon absorption

F , is the photon flux (number of photons per unit area and time)

t , is the time.

In a similar manner, the rate equation for two-photon absorption can be written as follows, keeping in mind that two photons are needed to produce one excited molecule:

$$\frac{dN_{TP}}{dt} = \frac{1}{2}\delta N_{GS} F^2$$

where,

δ , is the two-photon absorption cross section

N_{TP} , is the number of atoms/molecules per unit volume in the excited state due to two-photon absorption.

This shows that the probability of two-photon absorption depends on the square of the photon flux (or, equivalently, to the square of the light intensity). The two-photon cross-section is usually quoted in the units of Goeppert-Mayer (GM) (after its discoverer, Nobel laureate Maria Goeppert-Mayer), where 1 GM is 10^{-50} cm^4•s•$photon^{-1}$. Considering the reason for these units, one can see that it results from the product of two areas (one for each photon, each in cm^2) and a time (within which the two photons must arrive to be able to act together).

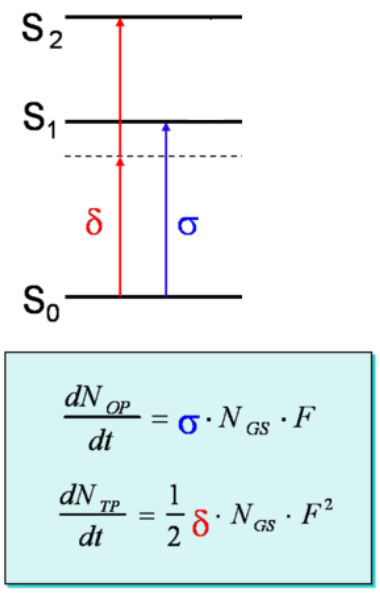

Figure 2.2: Schematic representation of one and two photon absorption indicating the cross section for each transition. S_o represents the ground state, S_1 and S_2 are the first and second real excited states. The dashed line corresponds to a virtual state.

For OPA with light intensity being a function of path length x or cross section being a function of concentration of the compound (in solution) c and the initial light intensity I_0, the Beer's law is described by the equation,

$$I(x) = I_0 e^{-acx}$$

and for TPA changes to,

$$I(x) = \frac{I_0}{1 + \beta c x I_0}$$

The absorption coefficient α now becomes the TPA coefficient β.

2.1.1 Optical damage

A topic of great practical importance is optically induced damage of materials. Optical damage is important because it ultimately defines the maximum amount of power that can be transmitted through a particular optical material. Optical damage thus imposes a constraint on the efficiency of many nonlinear optical processes by defining the maximum field strength E that can be used to excite the nonlinear response without the occurrence of optical damage. It is worth pointing out that present laser technology can produce laser beams of sufficient intensity to exceed the damage thresholds of all known materials. There are several different physical mechanisms that can lead to optically induced damage. These mechanisms, and an approximate statement of the conditions under which each might be observed, are as follows:

- Linear absorption, leading to localized heating and cracking of the optical material. This is the dominant damage mechanism for continuous-wave and long-pulse (≥1 μsec) laser beams.
- Avalanche breakdown, which is the dominant mechanism for pulsed lasers (shorter than ≤1 μsec) for intensities in the range of 10^9 W/cm^2 to 10^{12} W/cm^2.
- Multiphoton ionization or multiphoton dissociation of the optical material, which is the dominant mechanism for intensities in the range 10^{12} to 10^{16} W/cm^2.
- Direct (single cycle) field ionization, which is the dominant mechanism for intensities >10^{20} W/cm^2.

When a collimated laser beam interacts with an optical material, optical damage usually occurs at a lower threshold on the surfaces than in the interior. This observation suggests that

cracks and other imperfections on an optical surface can serve to initiate the process of optical damage, either by enhancing the local field strength in regions near the cracks or by providing a source of nearly free electrons needed to initiate the avalanche breakdown process. It is also observed (Lowdermilk and Milam, 1981) that surface damage occurs with a lower threshold at the exiting surface than at the entering surface of an optical material. One mechanism leading to this behavior results from the nature of the electromagnetic boundary conditions at a dielectric/air interface, which lead to a de-enhancement in field strength at the entering surface and an enhancement at the exiting surface. Another physical mechanism that leads to the same sort of front/back asymmetry is diffraction from defects at the front surface which can lead to significant intensity variation (hot spots) at the exiting surface[53].

2.2 Theory of Raman Spectroscopy

The main spectroscopies employed to detect vibrations in molecules are based on the processes of infrared absorption and Raman scattering. They are widely used to provide information on chemical structures and physical forms, to identify substances from the characteristic spectral patterns (‘fingerprinting’), and to determine quantitatively or semi-quantitatively the amount of a substance in a sample. Samples can be examined in a whole range of physical states; for example, as solids, liquids or vapours, in hot or cold states, in bulk, as microscopic particles, or as surface layers.

The interaction of light with a medium results in several processes: absorption, transmission and reflection for the most part, but, for a tiny fraction of the incoming light, scattering occurs due to inhomogeneities inside the medium. Those can be static for instance due to crystal dislocations, generating elastic scattering (i.e. with no change of wavelength), or dynamic such as atomic vibrations which produces a change in the wavelength. Only a tiny part of the light is inelastically scattered.

Raman spectroscopy is a technique based on the analysis of the inelastically scattered light from the medium, produced by the interaction of the light with the atomic vibrations. Usually, in a Raman spectroscopy experiment, the shift in energy between the incoming and inelastically scattered light is measured. The Raman effect was first observed in molecules by C.V. Raman in 1930, and nowadays Raman spectroscopy is a standard technique for the analysis of molecules, crystals and semiconductors[54]. In the macroscopic description of the

Raman scattering process in crystals, we consider an infinite crystalline medium at finite temperature. The atoms of the structure undergo vibrations, whose normal modes are quantized by quasiparticles called phonons.

When a molecule is positioned in an electric field *E*, an electric dipole moment *p* is induced. The relation between this induced dipole moment and the electric field can be expressed as a power series:

$$p = a \cdot E + \left(\frac{1}{2}\right) \cdot \beta \cdot E^2 + \left(\frac{1}{6}\right) \cdot \gamma \cdot E^3 \ \ldots \tag{2.2.1}$$

In this equation, α, β and γ are tensors, which are named polarizability, hyperpolarizability and 2nd hyperpolarizability, respectively. Typically, they are in the range of, $a \sim 10^{-40}$ C • V^{-1} •m^2, $\beta \sim 10^{-50}$ C•V^{-2} •m^3 and $\gamma \sim 10^{-60}$ C • V^{-3} • m^4. As these tensors each are a factor 10 billion less intense, the influence of these factors can in many cases be neglected. The induced dipole moment can be thus considered as directly proportional to the electric field and Equation (2.2.1) is reduced to:

$$p = a \cdot E \tag{2.2.2}$$

When studying the Raman effect, the electric field is caused by electromagnetic radiation. Indeed, light can be considered as an oscillating electric field. The electric field vector *E* on the moment *t* is described as:

$$E = E_0 \cdot \cos\left(2\pi \cdot \nu_0 \cdot t\right) \tag{2.2.3}$$

with ν_0 the frequency of the electromagnetic radiation.

In Equation (2.2.2) the polarizability α is a tensor, which is dependent on the shape and dimensions of the chemical bond. Considering that chemical bonds change during vibrations, the polarizability is dependent on the atomic/molecular vibrations. The polarizability tensor, *a*, is dependent on the normal coordinate *Q* of the atom/molecule. which is a generic vibrational coordinate (e.g. *r* for a stretch, *q* for a bend, etc). This relationship can be expressed as a Taylor series:

$$a = a_0 + \sum_k \left(\frac{\partial a}{\partial Q_k}\right)_0 \cdot Q_k + \frac{1}{2}\sum_{k,l}\left(\frac{\partial^2 a}{\partial Q_k \partial Q_l}\right)_0 \cdot Q_k \cdot Q_l + \ \ldots \qquad (2.2.4)$$

Q_k and Q_l are the normal coordinates that correspond with the k^{th} and l^{th} normal vibration, corresponding to the vibrational frequencies ν_k and ν_l .

In a first approximation, only the first two terms in this equation are maintained. This means that the different (normal) vibrations are considered as totally independent and no cross-terms are included in the equation. Thus, considering the ν^{th} normal vibration, Equation (2.2.4) is reduced to:

$$a_\nu = a_0 + a'_\nu \cdot Q_\nu \qquad (2.2.5)$$

, with a_ν the derivative of the polarizability tensor to the normal coordinate Q_ν, under equilibrium conditions.

In a first approximation, the normal coordinate oscillates according to the harmonic oscillator. The normal coordinate varies as a function of time according to:

$$Q_\nu = Q_{\nu 0} \cdot cos(2\pi \cdot \nu_\nu \cdot t + \varphi_\nu) \qquad (2.2.6)$$

with $Q_{\nu 0}$ the amplitude of the normal vibration and φ_ν a phase angle. Substitution of Equation (2.2.6) to Equation (2.2.5) gives:

$$a_\nu = a_0 + a'_\nu \cdot Q_{\nu 0} \cdot cos(2\pi \cdot \nu_\nu \cdot t + \varphi_\nu) \qquad (2.2.7)$$

When considering only the first two terms of the Taylor series (2.2.4), we assume that the polarizability tensor undergoes a harmonic oscillation, with a frequency ν_ν, that equals the vibrational frequency of the normal coordinate of the molecule. By substituting equations (2.2.7) and (2.2.3) in the (simplified) definition of the dipole moment *p* (Equation (2.2.2)), we obtain:

$$p = a_0 \cdot E_0 \cdot \cos(2\pi \cdot \nu_0 \cdot t) + a'_\nu \cdot E_0 \cdot Q_{\nu 0} \cdot cos(2\pi \cdot \nu_\nu \cdot t + \varphi_\nu) \cdot \cos\,(2\pi \cdot \nu_0 \cdot t) \qquad (2.2.8)$$

By using the trigonometrical formula:

$$cosA \cdot cosB = \frac{1}{2}[\cos(A+B) + \cos(A-B)] \tag{2.2.9}$$

equation (2.2.8) can be modified to:

$$\begin{aligned} p &= a_0 \cdot E_0 \cdot \cos(2\pi \cdot \nu_0 \cdot t) \\ &+ \frac{1}{2} a'_\nu \cdot E_0 \cdot Q_{\nu 0} \cdot \cos[2\pi \cdot (\nu_0 + \nu_\nu) \cdot t + \varphi_\nu] \\ &+ \frac{1}{2} a'_\nu \cdot E_0 \cdot Q_{\nu 0} \cdot \cos[2\pi \cdot (\nu_0 - \nu_\nu) \cdot t - \varphi_\nu] \end{aligned} \tag{2.2.10}$$

Therefore, we can consider the induced dipole moment as a function of the vibrational frequencies of the molecule (ν_ν) and of the incident radiation (ν_0):

$$p = p(\nu_0) + p(\nu_0 + \nu_\nu) + p(\nu_0 - \nu_\nu) \tag{2.2.11}$$

The induced dipole moment can be split into 3 components, each with a different frequency-dependence. The first term in Equation (2.2.11) corresponds to the elastic scattering of the electromagnetic radiation: the induced dipole moment has the same frequency (hence the same energy) as the incoming radiation. This type of scattering is called 'Rayleigh scattering', named after Lord Rayleigh (1842–1919), who used Rayleigh scattering to determine the size of an atom/molecule. The 2nd and 3rd term in Equation (2.2.11) correspond to the inelastic scattering of light. i.e. Raman scattering. In particular, the 2nd term corresponds to a higher energy of the scattered radiation, compared to the incident beam (Anti-Stokes scattering or shift), while the last term represents a lowering of the frequency (Stokes scattering or shift, Fig.2.3).

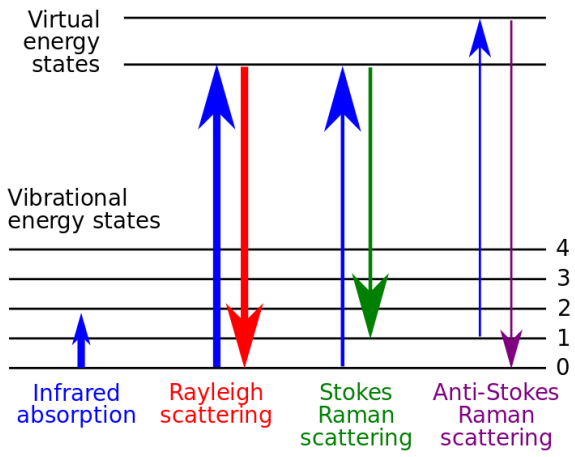

Fig. 2.3: Energy-level diagram showing the states involved in Raman signal. The line thickness is roughly proportional to the signal strength from the different transitions.

For anti-Stokes processes, the initial state is an excited state whose population depends on the temperature of the medium and is therefore less populated than the ground states. The anti-Stokes part of the spectrum is therefore weaker than the Stokes one. Comparing the intensity ratio between the Stokes and the anti-Stokes radiation can actually be used as a method to determine the crystal temperature. At this point, it is necessary to mention that the intensity or power of a normal Raman peak depends in a complex way on the polarizability of the molecule, the intensity of the source, and the concentration of the active group. The power of Raman emission increases with the fourth power of the frequency of the source; however, advantage can seldom be taken of this relationship because ultraviolet irradiation may cause photodecomposition of the sample. Raman intensities are usually directly proportional to the concentration of the active species.

Considering the Raman selection rules, it is important to know that vibrations having a symmetric polarizability change do not appear in Raman spectrum. As a consequence, bending vibrations are not strong Raman modes, but symmetric stretches tend to be strong Raman modes. Figure 2.4 shows the simple example of the symmetric molecule CO_2. The three vibrational modes, the change in polarizability and the mode that is Raman active, is depicted. As mentioned above, *a* is the polarizability and *Q* is a generic vibrational coordinate (e.g. *r* for a stretch, θ for bend, etc).

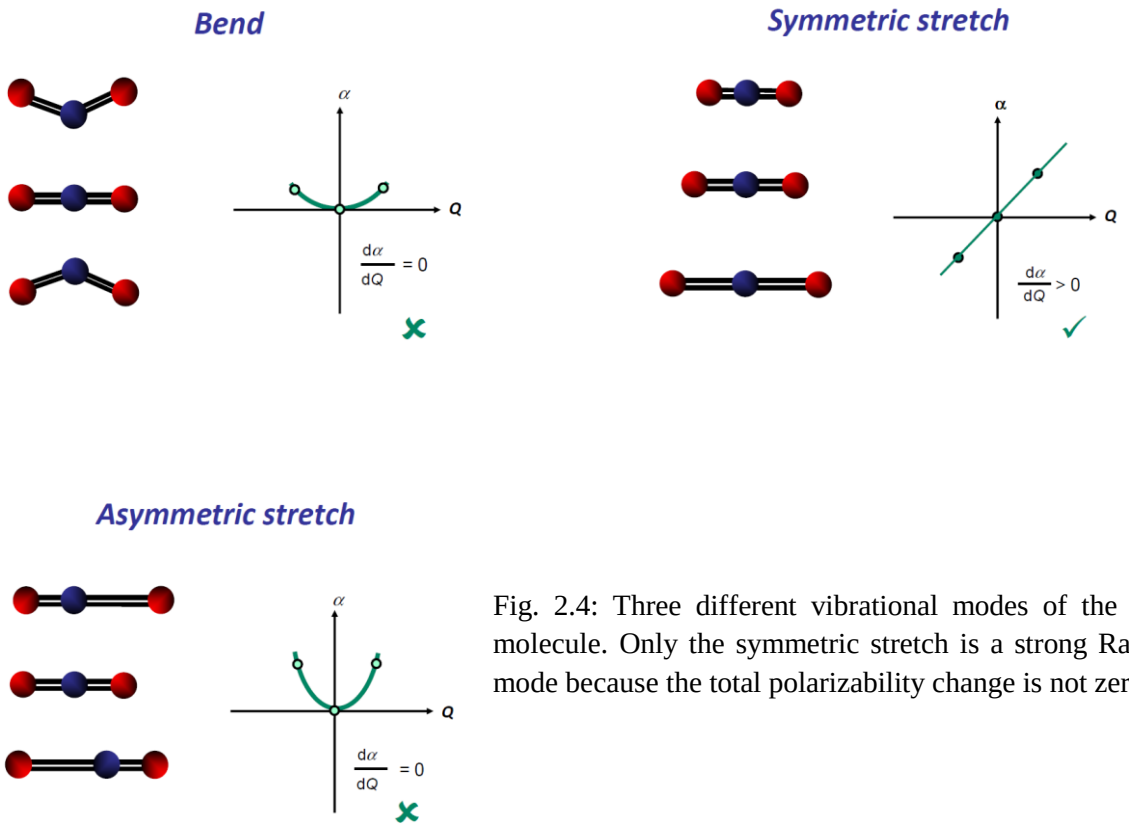

Fig. 2.4: Three different vibrational modes of the CO_2 molecule. Only the symmetric stretch is a strong Raman mode because the total polarizability change is not zero.

In case that one of the electronic states is real and not virtual, the Raman intensity of the peak corresponding to this process is enhanced by several orders of magnitude. This phenomenon is known as resonant Raman. Everything mentioned till this point is "first order" scattering, meaning the excitation of only one phonon. Two phonons also can be excited and this phenomenon is called "second order" scattering. Second order scattering is usually weak but can be enhanced by various processes.

2.2.1 Molybdenum disulfide phonon dispersion

In Raman spectroscopy, it is necessary to know the phonon dispersion in the reciprocal space for the crystal under investigation. The phonon dispersion of a crystal can be calculated by ab-initio density functional theory (DFT) or measured experimentally using neutron inelastic scattering spectroscopy. Figure 2.5 shows the results of the DFT calculation and the experimental results obtained by neutron scattering, for the bulk and single layer MoS_2. The overall agreement between theory and experiment is good[55]. The bulk phonon dispersion has three acoustic modes. Those that vibrate in-plane (longitudinal acoustic, LA, and transverse acoustic, TA) have a linear dispersion and higher energy than the out-of-plane acoustic (ZA) mode. The low frequency optical modes are found at 35.2 and 57.7 cm^{-1} and correspond to rigid-layer shear/vertical motion, respectively. When the wave number *q* increases, the acoustic and low frequency optical branches almost match. It is worth to mention the absence of degeneracies at the high symmetry points M and K and the two crossings of the ZA and TA branches just before and after the M point. The high frequency optical modes are separated from the low frequency modes by a gap of 49 cm^{-1} at the M and K points of the Brillouin zone. The Raman active modes are indicated in the phonon dispersion of figure 2.5. The atomic displacements of the Raman active modes (E^1_{2g} and A_{1g}) and the infrared active mode E_{1u}, are drawn in Fig. 2.6. The in-plane modes E^1_{2g} and E_{1u} are slightly split in energy (by 3 cm^{-1}). For the single-layer phonon dispersion, shown in Fig. 2.5, there is no longer a center of inversion as in the bulk. The number of phonon branches is reduced to nine. The single-layer and bulk phonon dispersions have a remarkable resemblance. In the bulk, all single layer modes are split into two branches but since the inter-layer interaction is weak, the

splitting is very low. The only notable exception from this is the splitting of the acoustic modes around Γ. In the single-layer, the resulting low frequency optical modes are absent.

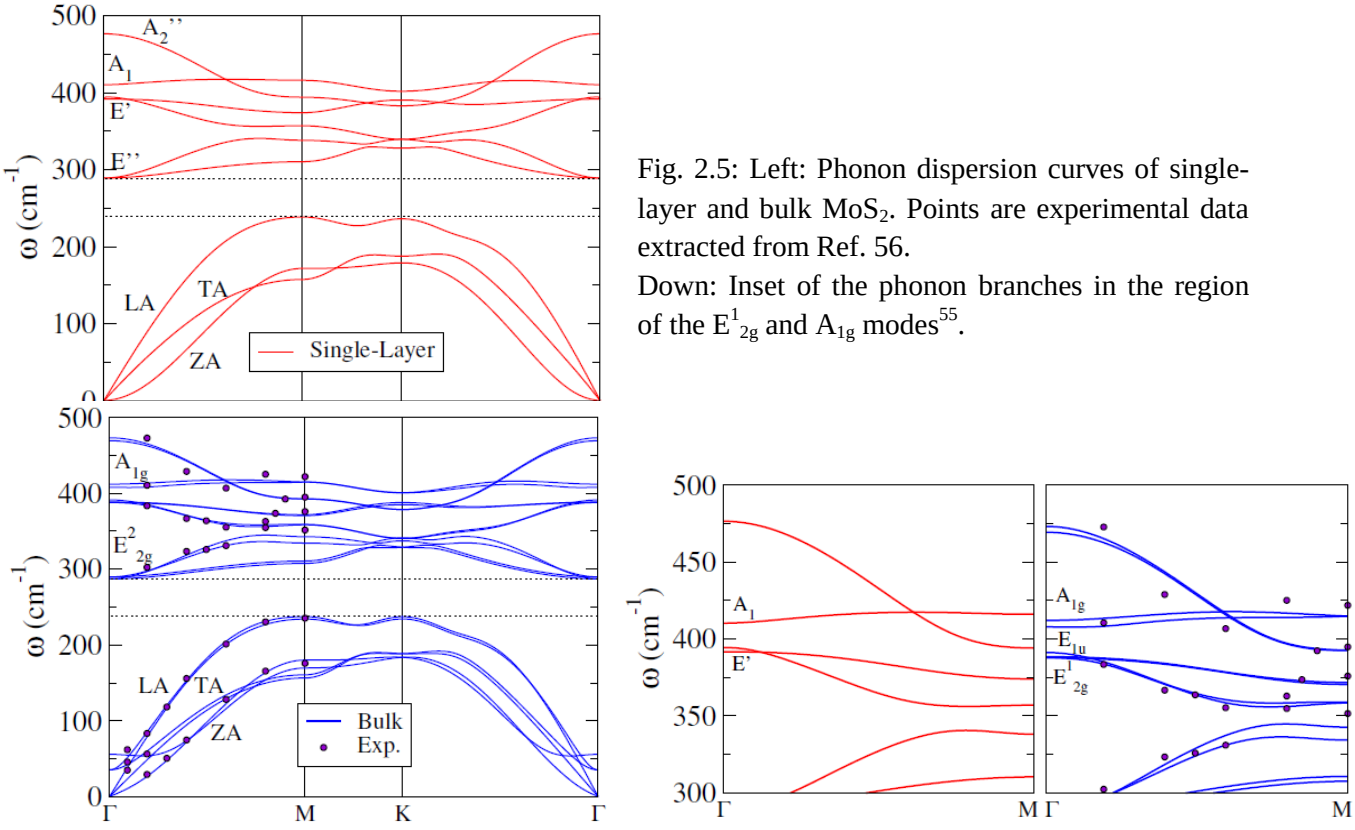

Fig. 2.5: Left: Phonon dispersion curves of single-layer and bulk MoS_2. Points are experimental data extracted from Ref. 56.
Down: Inset of the phonon branches in the region of the E^1_{2g} and A_{1g} modes[55].

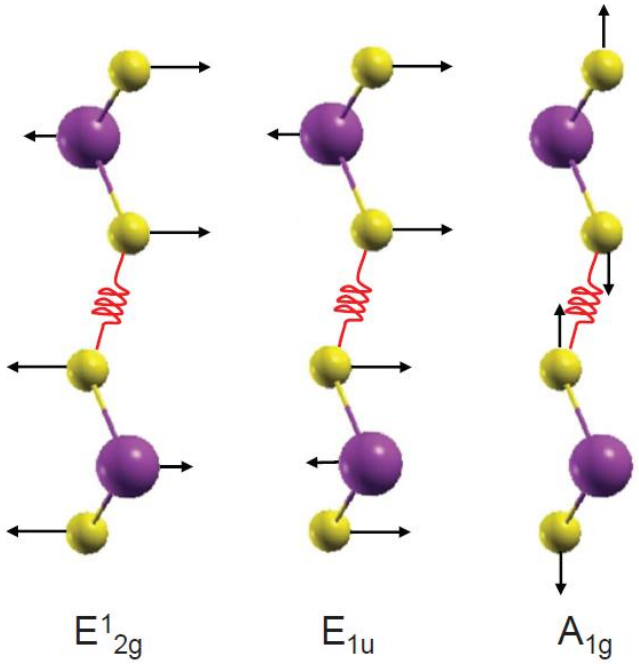

Fig. 2.6: Phonon modes in-plane E^1_{2g}, E_{1u}, and the out-of-plane phonon mode A_{1g}, for the bulk MoS_2.

2.2.2 Raman spectroscopy of Molybdenum disulfide

The Raman scattering spectrum of the bulk MoS_2 recorded at ambient temperature is shown in Fig. 2.7 along with the associated mode assignments. The A_{1g} mode at 407 cm^{-1} is an intralayer mode involving the motion of S atoms along the c axis. The E^1_{2g} mode at 382cm^{-1} is an intralayer vibrational mode involving motion of Mo-S atoms in the basal plane. The peak at 286cm^{-1} with weak intensity and E_{1g} symmetry is observed, which involves S atoms in the basal plane. This mode is forbidden in backscattering geometry. Nevertheless, it is observed most probably due to the disorder in the system. The spectrum of the pure 2H-MoS_2 exhibits a rigid-layer (RL) mode E^2_{2g} at 32cm^{-1}. This mode is of interlayer type involving rigid motion of neighboring sandwiches in anti-phase. In layered crystals, the frequency of the RL mode provides direct information on the strength of the interlayer forces in these crystals, since for such RL motions the restoring forces are provided entirely by layer-layer interactions.

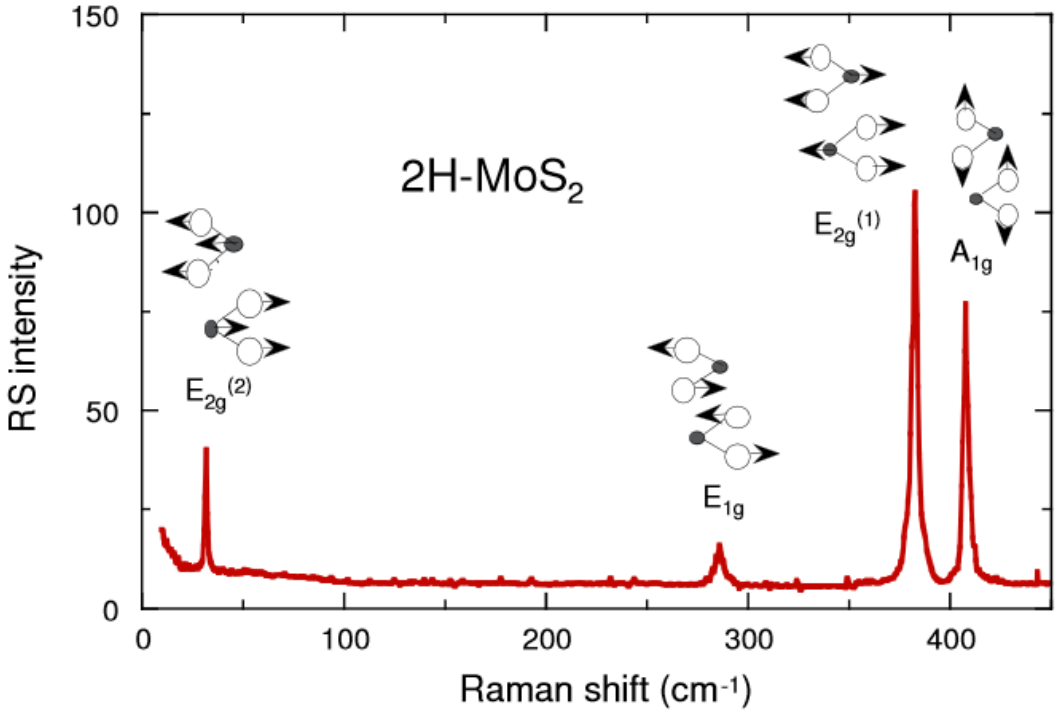

Fig. 2.7: Raman scattering spectrum of bulk 2H-MoS_2 crystal. The interlayer shear mode observed at 33.5cm^{-1} is typical of the trigonal prismatic structure[57].

A strong characteristic, the MoS_2 crystal exhibits, is the change of the frequency of Raman modes with the layer thickness. For all film thicknesses, the Raman spectra show strong signals from both the in-plane E^1_{2g} and the out-of-plane A_{1g} vibration. The behavior as a

function of film thickness has several intriguing characteristics. Most strikingly, (Figure 2.8a,b) the E^1_{2g} vibration softens (red shifts), while the A_{1g} vibration stiffens (blue shifts) with increasing sample thickness. For films of four or more layers, the frequencies of both modes converge to the bulk values. The rate of frequency change is twice as large for the A_{1g} as for E^1_{2g} mode. Spatial maps of the Raman frequency for the E^1_{2g} (Figure 2.8c) and A_{1g} mode (Figure 2.8d) clearly show these opposing shifts with layer thickness. The maps also demonstrate that the frequencies of the two modes have only very slight variation for different locations within a sample of a given layer thickness. This permits the Raman frequencies to be used as an indicator of the layer thickness[58].

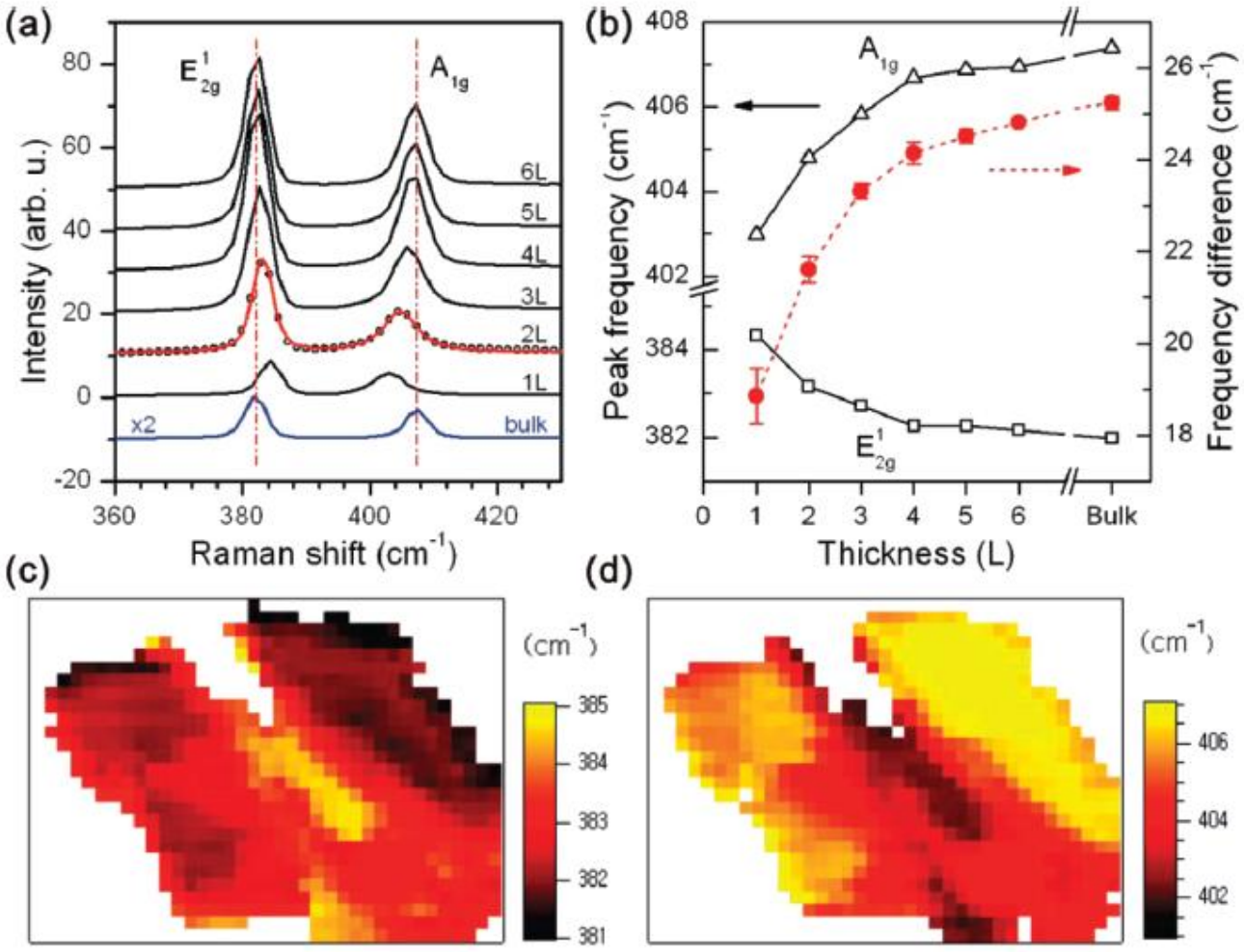

Fig. 2.8: (a) Raman spectra of thin and bulk MoS_2 films. (b) Frequencies of E^1_{2g} and A_{1g} Raman modes (left vertical axis) and their difference (right vertical axis) as a function of layer thickness. (c,d) Spatial maps (23 μm X 10 μm) of the Raman frequency of E^1_{2g} (c) and A_{1g} modes (d) for the sample shown on the right (dashed square)[58].

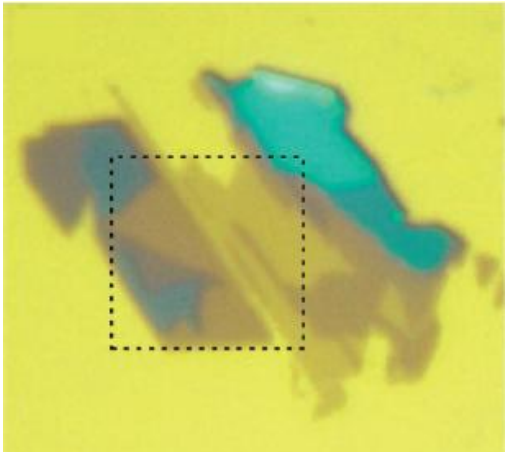

Within a classical model for coupled harmonic oscillators[59], the E^1_{2g} and A_{1g} modes are expected to stiffen as additional layers are added to form the bulk material from individual layers because the interlayer van der Waals interactions increase the effective restoring forces acting on the atoms. While the shift of A_{1g} mode observed with increasing layer number agrees with this prediction, the behavior of the E^1_{2g} mode does not. The failure of the model could reflect the presence of additional interlayer interactions; it could also indicate that the implicit assumption that stacking does not affect intralayer bonding is incorrect. Regarding the latter, a low-energy electron diffraction study of MoS_2 single crystals[60] showed that the interplane distance between Mo and S atomic planes within the topmost layer shrinks by ~5% compared to its bulk value. The lateral lattice expansion observed for dispersed single layers[61] may also be related to surface reconstruction. In addition, the A_{1g} mode of the topmost layer of bulk MoS_2 crystals[62] was found to soften by 25 cm^{-1}, possibly because of the surface reconstruction. The observed surface reconstruction and vibrational softening show that even the nominally weak interlayer interaction in MoS_2 can affect intralayer bonding and lattice dynamics.

Another seemingly perplexing feature is that the Raman intensities from single layers are stronger than from bulk MoS_2 samples (Figure 2.8). With increasing thickness, the intensities rise roughly linearly up to four layers and then decrease for thicker samples. A similar enhancement in the Raman intensity has been reported for graphene deposited on SiO_2/Si substrates where the maximum intensity occurs for ~10 layers[63]. As in the case of the graphene layers[63], much of this effect is clearly attributable simply to optical interference occurring for both the excitation laser and the emitted Raman radiation. The presence of the oxide film above the silicon substrate leads to significant optical field enhancements. The importance of this optical interference effect is highlighted by the fact that single layer MoS_2 on quartz produced only 20% of the Raman signal observed for such samples deposited on the SiO_2/Si substrates. In addition, changes in the electronic structure of the MoS_2 samples with layer thickness[2] may also play a role in the observed variation of Raman intensities.

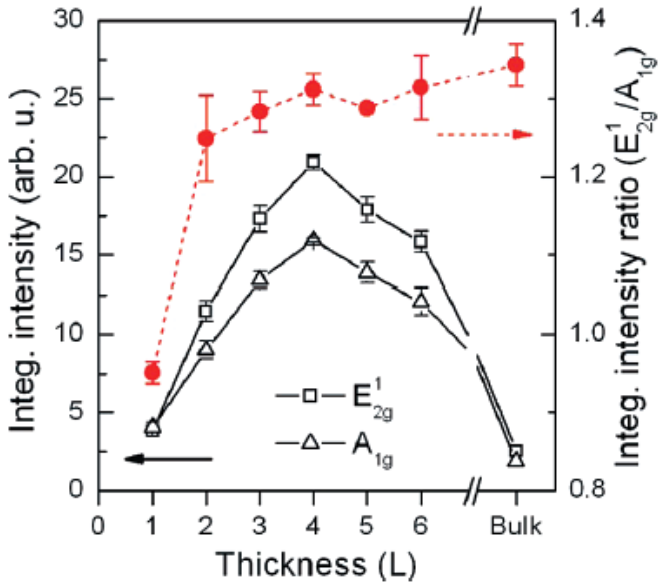

Fig. 2.9: Thickness dependence of integrated intensity (left vertical axis) and ratio of integrated intensity (right vertical axis) for the two Raman modes[58].

2.3 Conclusion

To conclude this Chapter, two-photon absorption is a nonlinear optical phenomenon that depends on the third order nonlinear optical susceptibility. Two-photon absorption in a material can be quantified via the two-photon absorption cross section, a quantity that is proportional to the imaginary component of the $\chi^{(3)}$ tensor and depends on the photon energy/energies. The probability of this optical phenomenon depends on the square of the light intensity. This is very important when studying the onset of the ionization or dissociation of an optical material, because multi photon absorption is the dominant mechanism for intensities in the range 10^{12} to 10^{16} W/cm^2, values that can be achieved using femtosecond pulses. Moreover, this chapter includes a simple theoretical analysis of Raman spectroscopy. The physical origin of the three induced dipole's moment components representing the anti-Stokes, the Stokes and the Rayleigh scattering, has been presented. The chapter focuses on the Molybdenum disulfide's Raman spectrum and describes its phonon dispersion calculations. The four Raman-active modes and their atomic vibrational representations are additionally shown. This chapter ends up with the frequency and intensity dependence of the in-plane E^1_{2g} and the out-of-plane A_{1g} Raman modes, on the thickness of the material.

CHAPTER 3

EXPERIMENTAL METHODS

3.1 Raman spectrometer

All the Raman spectra presented in this thesis have been measured by a Nicolet Almega XR Micro Raman analysis system. It consists of a confocal single monochromator spectrometer and it is equipped with a scanning motorized stage, an 100X Olympus objective lens with NA=0.9 and a 473nm diode-pumped solid-state laser (DPSS) with maximum output power of 50mW. The power of the incident beam is controlled with a neutral density filter and a high resolution grating (2400lines/mm) analyses the signal. The system is depicted in Fig. 3.1.

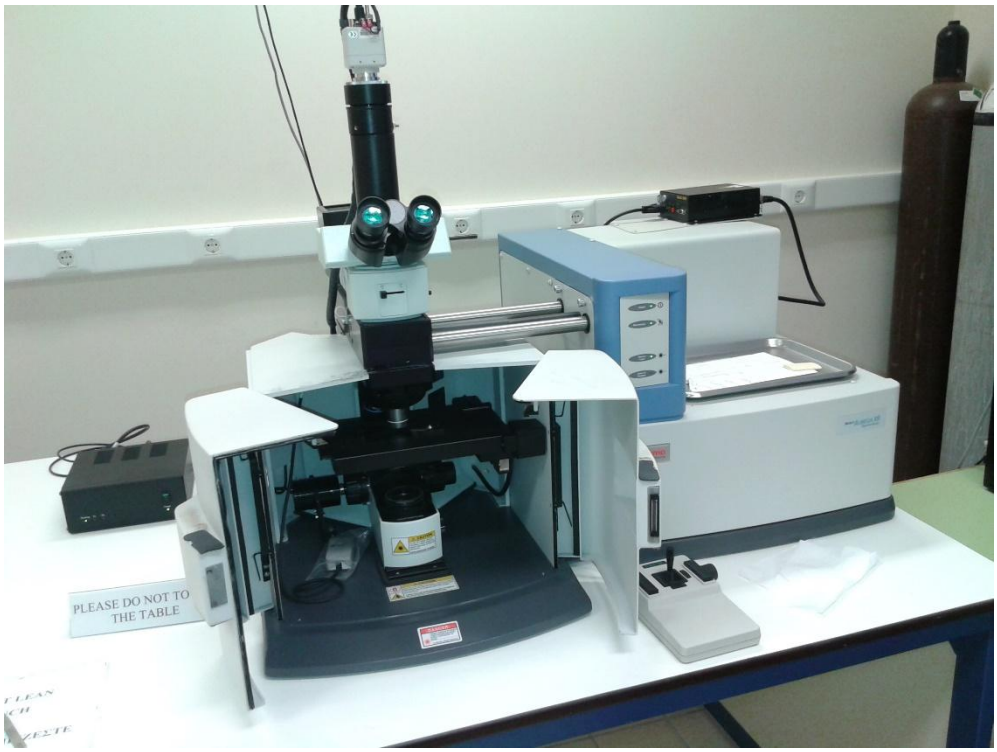

Figure 3.1: Nicolet Almega XR Micro Raman analysis system.

3.1.1 Confocal single monochromator spectrometer

A typical confocal Raman spectrometer is sketched in Figure 3.2. It is composed of three major parts: a laser, a microscope and a spectrum analyser. The microscope directs the laser beam onto the sample and redirects the back-scattered light to the analyser that records the energy spectrum of the scattered light. More specifically, the laser passes through a beam splitter and is focused onto a sample by an objective lens. The sample is mounted on a scanning XYZ motorized stage.

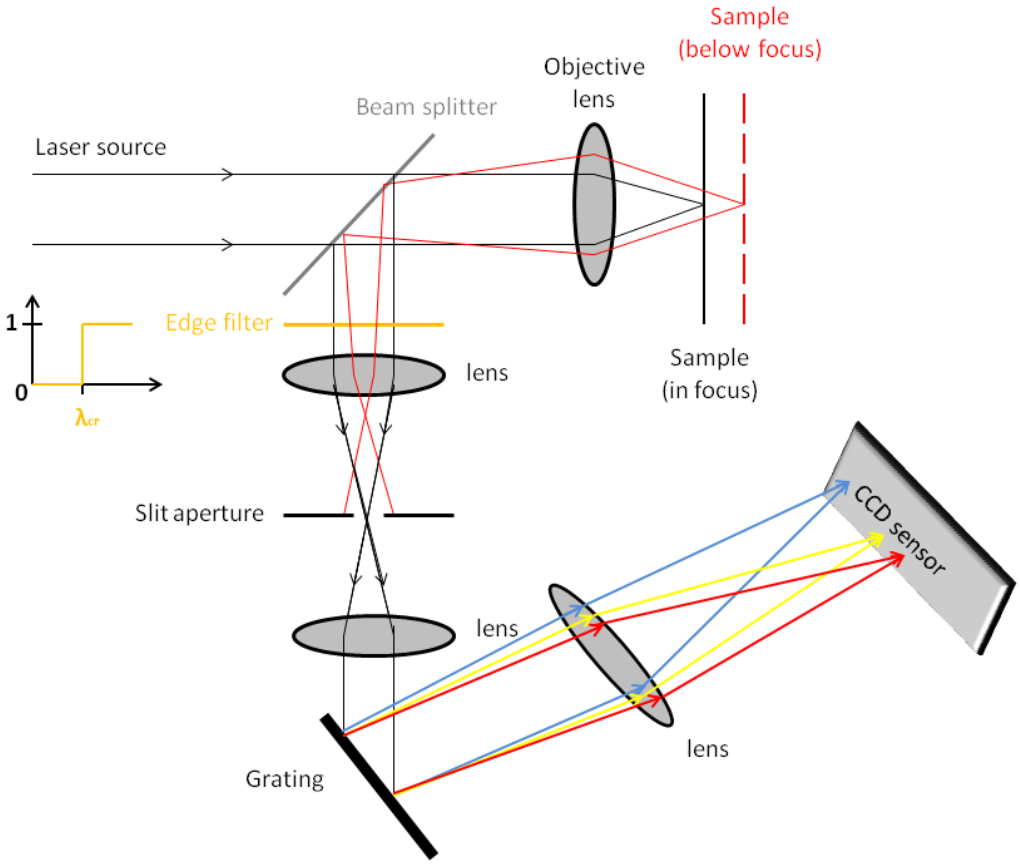

Figure 3.2: Sketch of a single monochromator Raman spectrometer

As the laser enters the sample, inelastic and elastic scattering occurs. Figure 3.2 depicts the reflected light path scattered at two different depths of the sample, one in the focal plane of the objective and the other one out of focus. After re-entering the microscope through the objective, both beams hit the beam splitter which now acts as a mirror. A longpass filter cuts out the Rayleigh emission, i.e. the elastically scattered light as it constitutes the major part of

the beam and could risk damaging the light detector. The beam splitter and edge filter can be realized by a specific single optical element called a dichroic mirror. It is transparent for light with a given energy until a certain threshold value after which it acts as mirror. After removal of the Rayleigh component, another lens focuses the beam on a slit aperture which cuts out the rays coming from different layers of the sample that are not in the focal plane of the objective. This is an important feature of a confocal spectrometer. It allows information to be obtained at a specific depth in the sample. The beam is then diffracted by a grating and re-focused onto a CCD sensor in the focal plane of the last lens. The CCD sensor converts the incoming photons into an electrical signal and accumulates counts between each read out on request from the software. The result is a spectrum with a number of counts assigned to each resolvable energy.

3.1.2 Spectral and energy resolution

Based on the description of the Raman beam path above, the definition of the different resolutions can be provided. First, the spatial resolution in XY is defined as half the size of the probe on the sample, i.e. the minimum laser spot size diameter after the objective. The minimum spot size that can be achieved is diffraction limited and is related to the diameter of the first Airy disc $d = 1.22 \lambda / NA$, where NA is the numerical aperture of the objective and λ the excitation wavelength. Thus the spatial resolution obtained with an (100x,NA=0.9)-objective and a 473nm laser used in our experiments, is ~ 650/2 = 325nm. The depth resolution is limited by the size of the slit aperture. A smaller slit aperture enhances the depth resolution but also decreases the total intensity of the signal. The value of the depth resolution greatly depends on the optical path and therefore on the spectrometer. Finally, the spectral resolution is related to the ability of the spectrograph to resolve small changes of photon energy. Thus it depends on the grating's diffraction capability and can be improved by increasing the density of the grating's grooves.

3.2 Sample preparation

Si substrates ([100], n-type, 700μm thickness) were cleaned following the RCA procedure. Then a silicon oxide layer was grown onto them via a high temperature-oxidation process performed for 5h at 1000^0C in air. Few-layer MoS_2 samples were mechanically exfoliated from a bulk natural crystal (SPI Supplies) using an adhesive tape and subsequently deposited on the Si/Silicon Oxide (290 nm) wafers. Single layer regions of 3–5 μm size were identified with an optical microscope and confirmed with micro-Raman (Thermo Scientific, Nicolet Almega XR) spectroscopy at room temperature. To further confirm the existence of monolayers, photoluminescence (PL) studies from 80K to 300K were employed using a micro-PL setup in backscattering geometry using a 532 nm continuous wave laser as an excitation source.

3.3 Irradiation setup

The irradiation experiments were performed using a Tsunami 200 femtoseconds (fs) Ti:Sapphire laser system operating at 800 nm wavelength and 1 kHz repetition rate. The energy of the beam was controlled via a combination of a waveplate, a linear polarizer, and a series of neutral density filters, while the polarization direction was controlled via a λ/2 waveplate. An iris aperture was used to obtain the central part of the beam and acquire a uniform energy distribution. A mechanical chopper was used to control the desired number of pulses interacted with the sample. The laser beam was focused down to 100 μm onto the sample, placed on an XYZ translation stage, at normal incidence. The alignment and irradiation processes could be continuously monitored by means of an imaging setup. The setup is depicted in figure 3.3. In a typical experiment, the laser beam irradiated monolayers adjacent to bulk areas in an effort to compare the response of such different areas upon excitation.

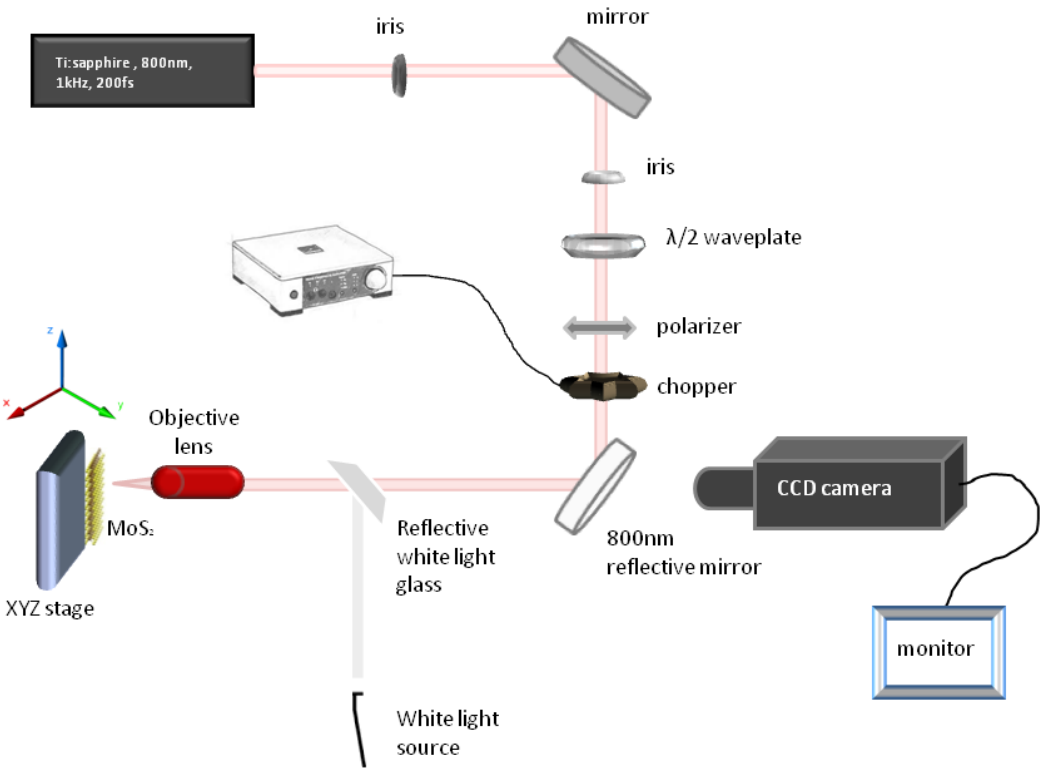

Figure 3.3: Femtosecond laser setup used for the irradiation of MoS_2 samples.

Part II
Experimental results

CHAPTER 4

FEMTOSECOND PHOTOEXCITATION OF BULK AND MONOLAYER MoS_2

4.1 Sample characterization

Figure 4.1(a) shows a typical optical microscopy image of exfoliated flakes, where areas of different layer numbers are indicated. AFM measurements revealed that the bulk thicknesses were ranging from 60nm to 80nm for several samples studied. Fig. 4.1(e) shows a typical AFM measurement of a bulk MoS_2 section. Micro-Raman spectroscopy, using the 473 nm excitation wavelength with very low intensity in order to avoid structural damage, was utilized to identify the number of layers in certain areas of the exfoliated flakes. The energy difference between the two most prominent Raman vibrational modes, A_{1g} and E^1_{2g}, is used extensively in the literature as the fingerprint of the number of layers;[58] This is extensively discussed in chapter 2.2.1. A_{1g} is the out-of-plane and E^1_{2g} is the in plane vibrational mode whose energy at the monolayer limit is 402 cm^{-1} and 384 cm^{-1}, respectively. Typical Raman spectra of single layer, bilayer, and bulk at T=300K are shown in Fig. 4.2(a). The low-energy shoulder is an artifact of the measurement apparatus since it is also observed in the Si Raman peak at 520 cm^{-1}. The energy difference of 18 cm^{-1} for the lower spectrum unambiguously confirms the single layer MoS_2. To further confirm the existence of monolayers, we have performed temperature dependent photoluminescence spectroscopy. The inset of Fig. 4.2(b) shows a typical PL emission spectrum taken at 80K using a 532 nm laser as an excitation source. The main peak of this spectrum is the strong PL emission at approximately 1.90 eV which is due to the direct A-exciton transition at the K-point of the Brillouin zone[2,6,7]. The temperature dependence of this feature, shown in Fig. 4.2(b), exhibits a standard semiconductor-like behavior and can be described by the Varshni relation (chapter 1.3). The solid line is a fit to the data using the values α=0.33 meV/K and β=238 K for the Varshni

parameters. These PL characteristics are in accordance with previous studies presented in the literature[7,64].

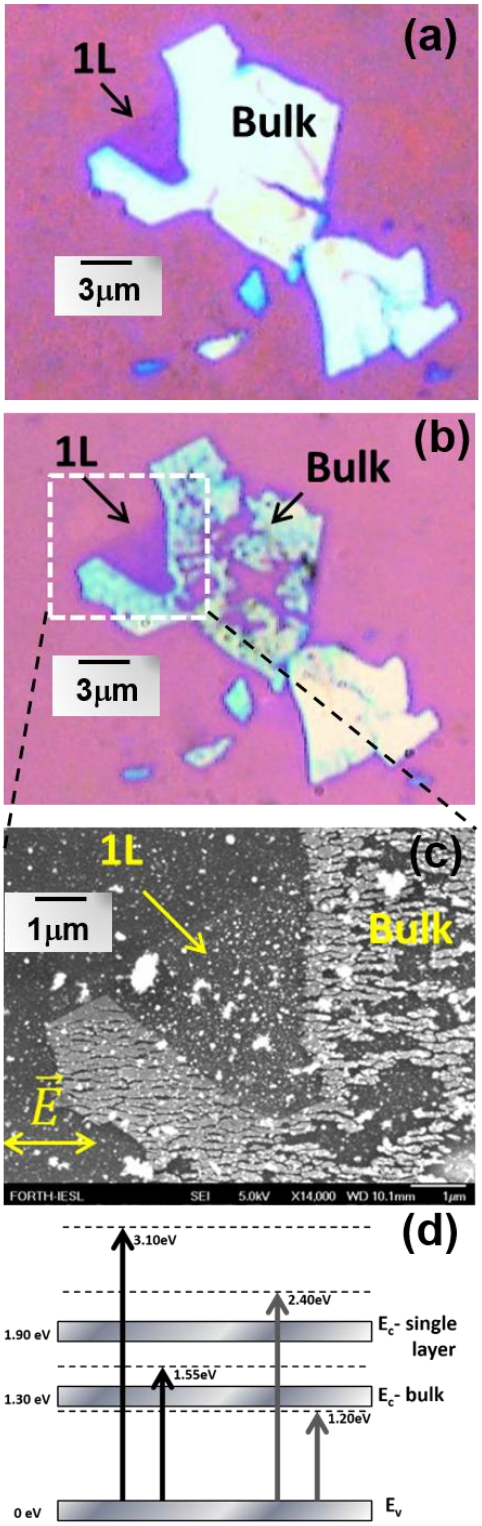

Fig. 4.1: (a) Optical microscope image of pristine bulk and single layer MoS_2 obtained by mechanical exfoliation on 290 nm Silicon oxide. (b) Optical microscope image of the sample irradiated by 20 mJ/cm^2 and 10^3-200 fs pulses of an 800 nm-1 kHz laser. (c) FESEM image of the sample (dashed line square region in Fig. 1(b)) irradiated by 20 mJ/cm^2 and 10^5 pulses. Ripple formation parallel to the electric field vector on bulk MoS_2 and single layer distortion. (d) Schematic representation showing the optical gap of bulk and monolayer MoS2 and the electron excitation via single and TPA process of 800 nm (1.55 eV) and 1030 nm (1.20 eV). (e) AFM profile of bulk MoS_2.

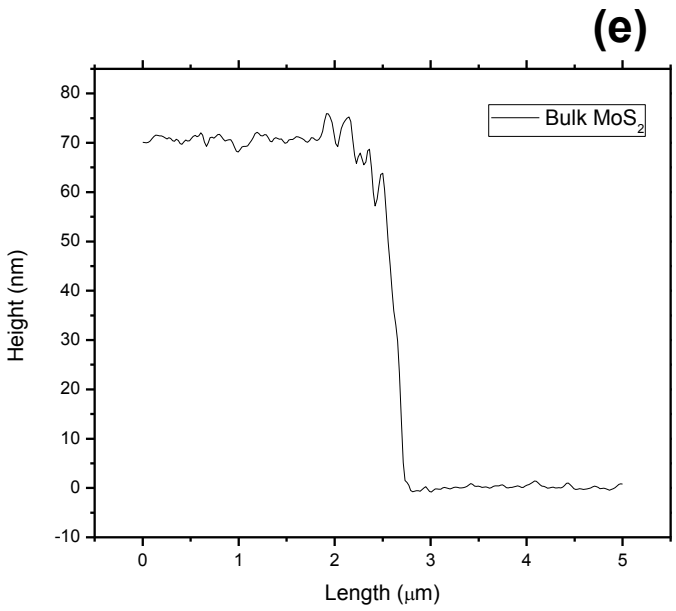

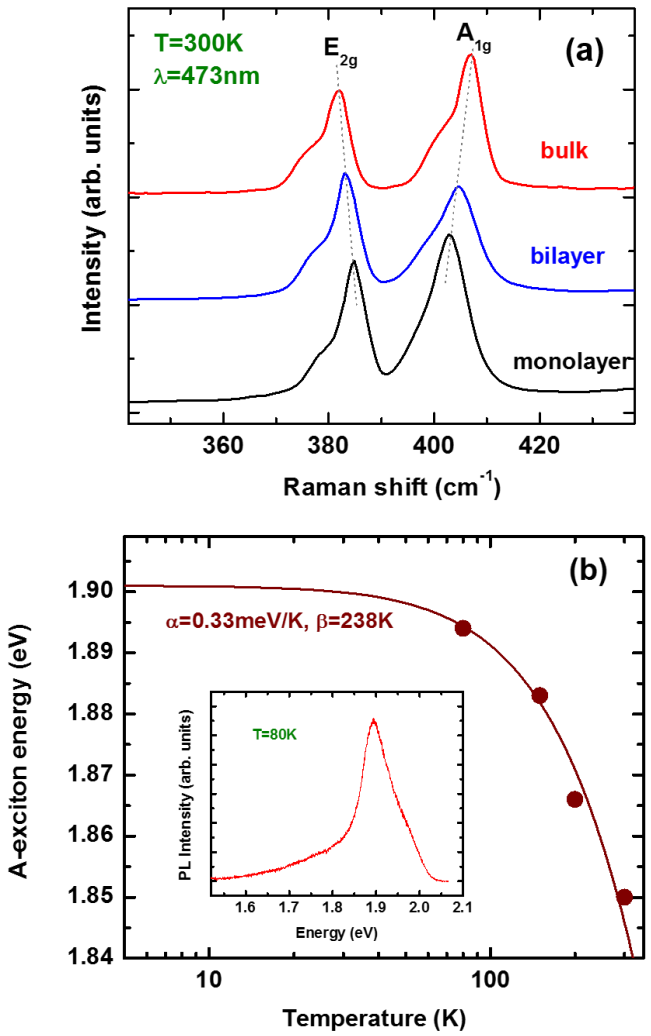

Fig. 4.2: (a) Raman spectra at T=300K for bulk, bilayer, and monolayer MoS_2. The energy separation between the in plane E^1_{2g} and the out of plane A_{1g} is 18 cm^{-1}, characteristic of single layer. (b)Temperature dependence of the photoluminescence taken with 532nm excitation shows a typical semiconductor behavior. The PL is dominated by the A-exciton emission (inset, PL at 80 K).

4.2 Optical damage of bulk and single layer MoS_2

We initially investigated a single-pulse optical damage threshold of monolayer MoS_2 and compare it with that of the bulk. We define such threshold as the single-pulse light flux at which submicron-sized distortion features are created in either of the two cases. We observed that the damage threshold of the monolayer is very well-defined, i.e., no modification is observed up to a certain fluence of 50 mJ/cm^2 (2.5 mW), beyond which damage occurs via material ablation. Interestingly, it is found to be higher than that of the bulk that is 15 mJ/cm^2 (750 μW). These values correspond to time averaged power. Figure 4.1(b) shows an optical microscopy image of MoS_2 bulk and monolayer flakes exposed to 10^3 pulses at a fluence of

20 mJ/cm^2 that is above the bulk damage threshold but below that of the monolayer. It is evident that while bulk areas were significantly distorted due to material ablation, the single layer was practically unaffected by laser irradiation. However, upon increasing the number of pulses to 10^5, while keeping the fluence at 20 mJ/cm^2, the monolayer can also be affected. This is confirmed by the respective field emission scanning electron microscopy (FESEM) image of Fig. 4.1(c), showing that the single layer is distorted as well.

4.2.1 Raman analysis

Raman spectroscopy was employed to investigate the characteristics of the lattice modifications induced in bulk and monolayer MoS_2 as a function of the irradiation intensity and total exposure time. A first observation was a significant decrease of the intensities of A_{1g} and E^1_{2g} Raman modes recorded from the ablated areas compared to the pristine ones while no energy shift of these peaks was observed. A similar effect has been observed during femtosecond laser interaction with graphene[65,66].

To further shed light on this effect, we monitored the evolution of the Raman spectra as function of the number of irradiation pulses N (proportional to the exposure time), using laser fluences below the single-shot damage threshold. We first irradiated the sample with the femtosecond laser, then we performed Raman measurements in a different experimental setup and then we irradiated the sample again at the same spot, repeating this process several times with different number of pulses each time. Fig. 4.3(a) (3(b)) show the dependence of the intensity for the out of plane A_{1g} (E^1_{2g}) mode to the number of pulses N for the monolayer and bulk at 600μW. This laser power is below the damage threshold for both bulk and monolayer. The data were normalized to the single pulse intensity (N=1). In case of the monolayer, the A_{1g} and E^1_{2g} peak intensities were practically constant with N until they rapidly decreased at a critical exposure time. Such abrupt decrease possibly indicates ablation and eventual sublimation of the MoS_2 lattice. On the other hand, for bulk MoS_2, a monotonic decrease of the A_{1g} and E^1_{2g} peak intensities was observed for low N followed by a more abrupt decrease than that recorded for the single layer. Compared to the monolayer, the latter occurred at lower number of irradiation pulses. Both of the above results comply with the lower optical damage threshold observed for the bulk compared to the single layer. It should be noted that the above results were repeatable within experimental uncertainty over different

probing sites within the bulk and/or monolayer areas. The inset of Fig. 4.3(a) (4.3(b)) shows Raman spectra for the A_{1g} (E^1_{2g}) mode for monolayer and bulk taken under N=1 and N=10^5 irradiation pulses. The plots clearly demonstrate the dramatic effect on the intensity that a large number of pulses has on the bulk with respect to the monolayer. Again, the spectra were normalized to the single pulse intensity (N=1).

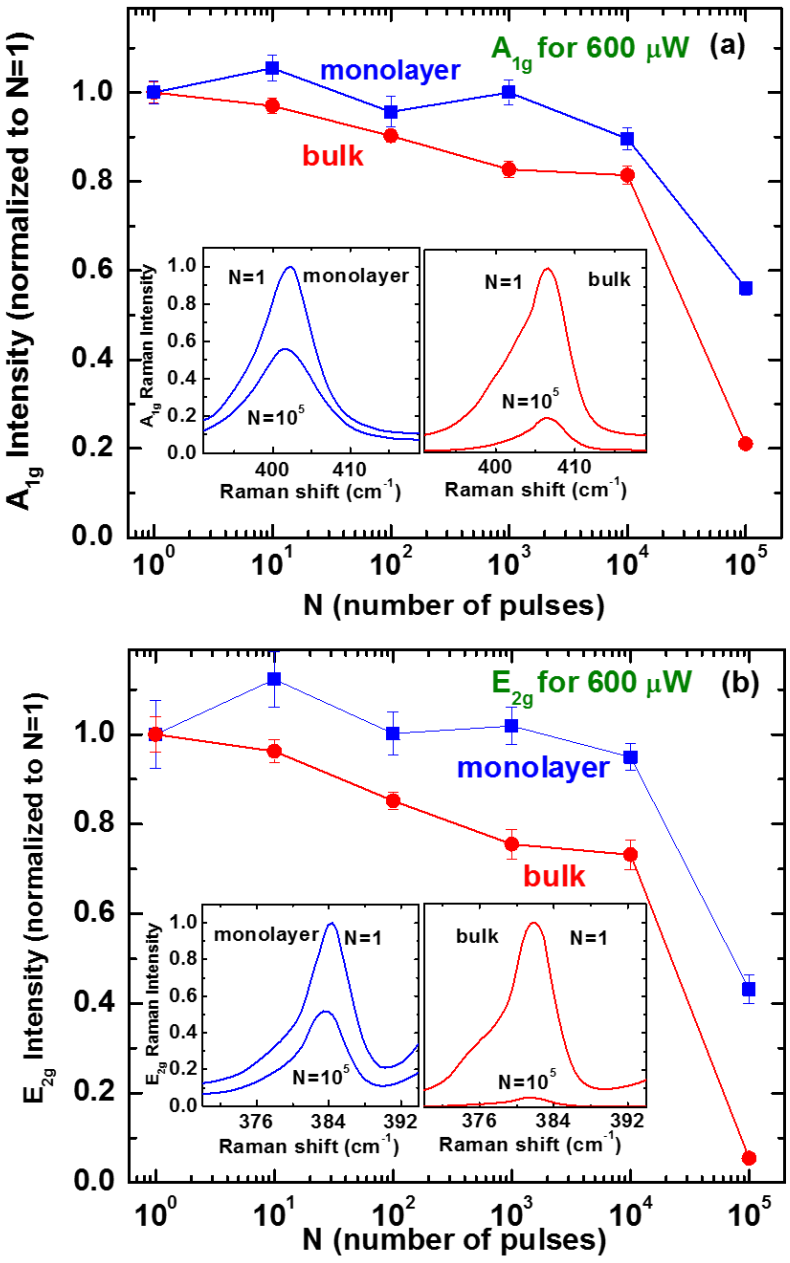

Fig. 4.3: Intensity of the out of plane A_{1g} (a) and in plane E^1_{2g} mode (b) as function of the number of pulses N for the monolayer and bulk at 600 μW (normalized to N=1). The inset shows the A1g (a) and E2g (b) Raman spectra for monolayer and bulk taken under N=1 and N=10^5 irradiation pulses.

Lorentzian fit analysis in our raw data showed that the linewidth of the two main Raman modes, as a function of the number of irradiation pulses, remains practically constant within the experimental error. This is demonstrated in Fig .4.4(a,b).

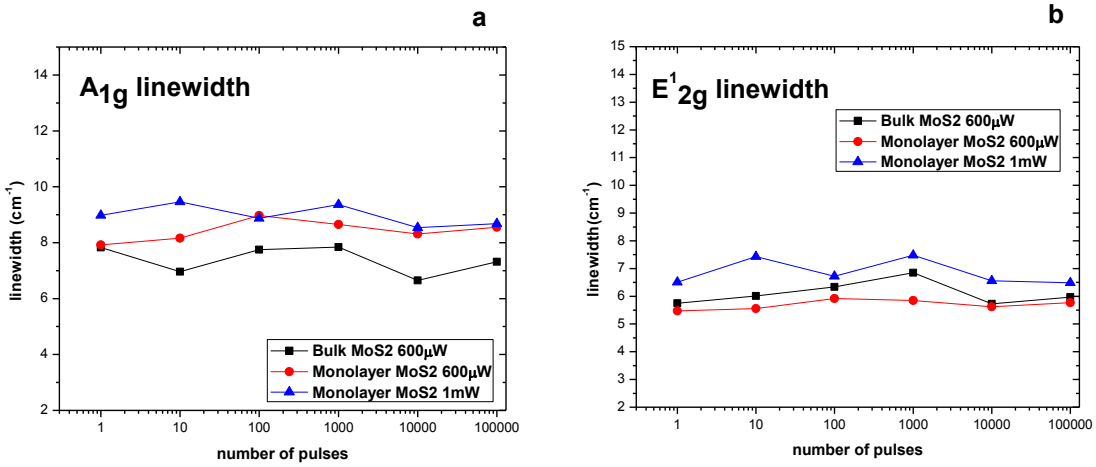

Fig. 4.4: (a) A_{1g} and (b) E^1_{2g} linewidth of the two main Raman modes as a function of the number of irradiation pulses. In both cases, the linewidth remains practically constant within the experimental error.

Figures 4.5 (a) and 4(b) present the pulse number dependence of the Raman peaks for the monolayer at two different fluences (12mJ/cm^2, i.e., 600 μW and 20 mJ/cm^2, i.e., 1mW, both below the single-shot single-layer damage threshold). It is evident that the peak intensity of both Raman modes is a strong function of the irradiation intensity.

We postulate that the observed weakening of the Raman peaks can be attributed to a corresponding decrease in the number of scattering centers (i.e., Mo-S bonds), possibly due to laser-induced bond breaking and subsequent atoms removal. Indeed, as N was increased, optical and FESEM microscopy revealed the formation of macroscopic holes within the flake area that progressively increased in size upon further exposure. This is in accordance to previous observations on radiation induced damage studies showing that as soon as the MoS_2 sheet is perforated by losing first a single S atom and subsequently the other Mo–bonded S atom via ionization, this hole readily enlarges[67].

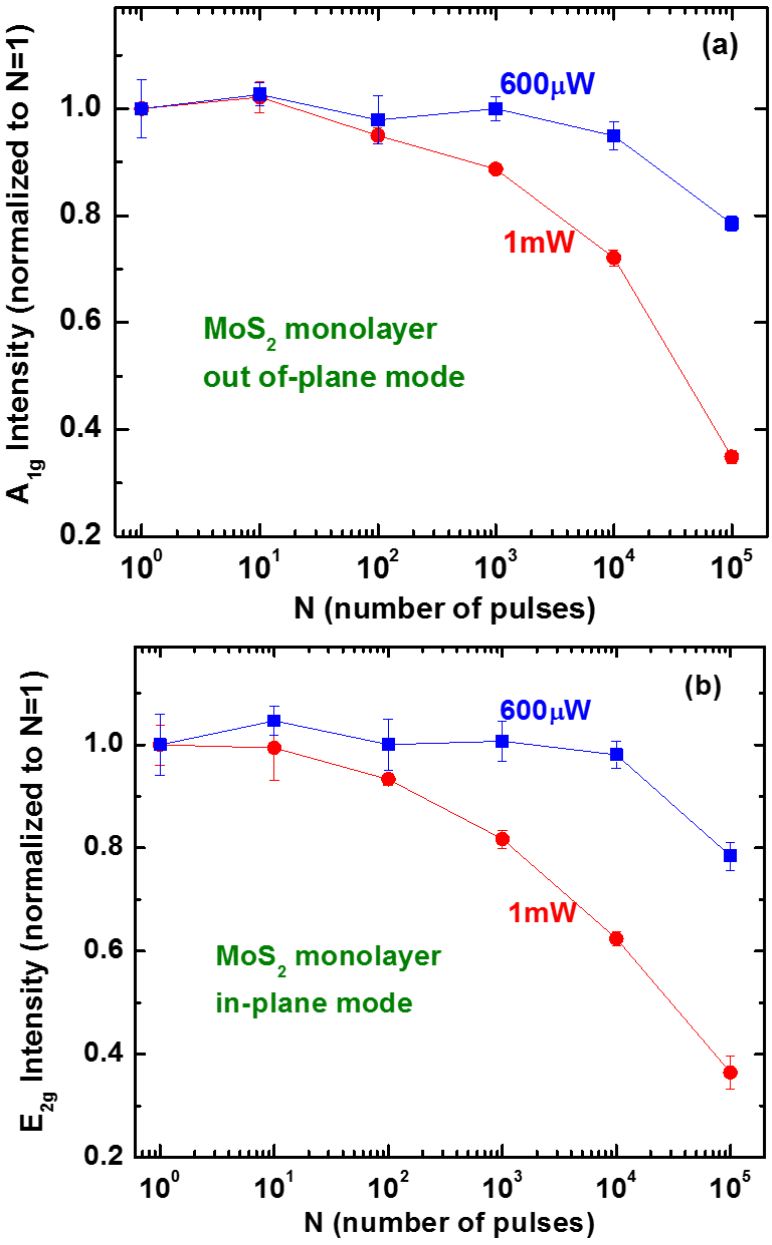

Fig. 4.5: Normalized (to N=1) intensity of the out of plane A_{1g} (a) and in plane E^1_{2g} mode (b) for the single layer as function of the number of pulses N at two different fluences.

It should be noted that the absence of a peak at 820 cm^{-1} in the Raman spectra of the irradiated areas, which is the fingerprint associated with the high-temperature oxidation of MoS_2 to MoO_3, suggests that the MoS_2 surface is not affected by oxidation during the laser irradiation process. Therefore, it can be proposed that the damage of nanosheets occurs through lattice sublimation. We performed experiments with a continuous wave (CW) laser of 532nm wavelength, using a fluence that is above the damage threshold of bulk MoS_2.

Raman study revealed that no oxidation occurred in the damaged areas of MoS_2 crystals, similar to the case of fs laser irradiation. Although this is unexpected, it is in agreement with similar experiments[68]. Indeed, in agreement to our data, this study showed that no oxidation occurred upon CW irradiation of natural MoS_2 crystal. This is in contrast with CW irradiation of microcrystalline MoS_2 powder which is heavily oxidized upon irradiation using the same conditions. It therefore seems that that the damage of natural MoS_2 occurs through lattice sublimation in both fs-pulsed and CW irradiation cases.

For the ultrafast matter interaction, electronic excitations should be significant in the timescale of hundreds of fs, due to the absence of electron-phonon coupling during the pulse. Under such conditions, electrons are excited from bonding to anti-bonding states while the energy due to recombination of photoexcited carriers facilitates photochemical bond breaking. Investigation of the dependence of laser induced lattice degradation process on pulse duration may assist towards understanding the photothermal and photochemical contributions. For this purpose, experiments comparing fs with longer pulses are included in future work.

4.2.2 Proposed mechanism

Optical breakdown and subsequent lattice distortion occur when photogenerated electron density in the conduction band reaches a critical value. The monolayer MoS_2 is a direct semiconductor with an optical gap of ~1.90 eV, while the bulk MoS_2 is an indirect semiconductor with an optical gap of ~1.30 eV. Considering the laser photon energy of 1.55 eV (λ=800 nm) used in our case, single-photon absorption dominates for the multilayer MoS_2, while monolayer can only be excited via a two-photon absorption (TPA) process (Fig. 4.1(d)) that shows a quadratic dependence on the laser intensity. One consequence of TPA-governed laser induced breakdown is an increase by more than three times of the damage threshold,[69] since the absorption of two photons is by orders of magnitude less probable than the single photon absorption process[70]. Therefore, in our case, the probability of reaching the critical electron excitation required for lattice decomposition is much lower in case of the larger-gap monolayer MoS_2. To further explore the above proposed mechanism, single-shot irradiation experiments were performed using a same repetition-rate laser source, with a photon energy of 1.20 eV (λ=1030 nm-Yb doped Potassium-Gadolinium Tungstate crystal)

which is below the gap of both the monolayer and the bulk. In this case, the single-shot damage threshold of monolayer and bulk MoS_2 were found to be comparable, i.e., 300 and 240 mJ/cm^2, respectively, as indeed anticipated due to the occurrence of TPA process in both cases. Unlike the small differences in the absorbance between 1.55 eV and 1.2 eV for monolayer MoS_2,[2] there is a six-time rise in the single-shot damage threshold. However, considering the non-linear nature of absorption process, small differences in the absorbance could correspond to a non-linear relation of the respective damage threshold differences.

Finally, it should be noted that the optical damage in bulk MoS_2 gives rise to interesting pseudo-periodic (period of ~200 nm) ripple-like patterns (Fig. 4.1(c)) oriented parallel to the laser polarization. Ripples' formation is commonly observed in semiconducting materials and can be mainly attributed to electromagnetic interference effects[71]. Formation of self assembled surface structures is an interesting aspect of the interaction of ultrafast lasers with 2D materials. Future experiments will investigate the physics behind the generation of the observed patterns in the case of MoS_2.

4.3 Conclusion

We have investigated the effect of intense femtosecond laser excitation on the structure of bulk and monolayer MoS_2. The evolution of A_{1g} and E^1_{2g} vibrational modes was recorded as a function of irradiation intensity and total exposure time. The observed behavior of the Raman peaks could be attributed to a corresponding decrease in the number of Mo-S bonds, possibly due to laser-induced bond breaking and subsequent atoms removal. Since no MoO_3 formation was observed in the Raman spectra, it can be proposed that the damage of nanosheets occurs through lattice sublimation. The single-pulse optical damage threshold was determined for the monolayer and bulk to be 50 mJ/cm^2 and 15 mJ/cm^2, respectively, under 800 nm wavelength irradiation. The more than 3 times higher damage threshold for the monolayer is understood as the result of a two-photon absorption process versus single-photon absorption in the bulk. This mechanism was verified under a higher wavelength (1030 nm) irradiation where two-photon absorption is required not only for the single layer but also for the bulk.

Part III:
Conclusion and future plans

5. Future work and perspectives

This thesis discussed about the interaction of fs laser pulses with the MoS_2 crystal. In chapter 4.2.1 we discussed the mechanism of the interaction in the timescale of hundreds of fs. The dependence of laser induced lattice degradation process on pulse duration needs extensive investigation in order to understand the photothermal and photochemical contributions. Experiments using picosecond and nanosecond lasers as well as pump-probe studies of the dynamics of the degradation process are included in future work.

In chapter 4.2.2 we have shown that the optical damage in bulk MoS_2 gives rise to interesting pseudo-periodic (period of ~200 nm) ripple-like patterns (Fig. 4.1(c)) oriented parallel to the laser polarization. Ripples' formation is commonly observed in semiconducting materials and can be mainly attributed to electromagnetic interference effects[71]. Formation of self assembled surface structures is an interesting aspect of the interaction of ultrafast lasers with 2D materials. Future experiments will investigate the physics behind the generation of the observed patterns in the case of MoS_2. A deep study that controls the number of pulses, the fluence and the pulse duration will reveal the correlation of these parameters with the ripple formation and will help understand the mechanism behind electromagnetic interference effects.

A challenging future plan is the detailed investigation of the vibrational and optical properties of the Germanium Selenide (GeSe) crystal. This 2D crystal has an orthorhombic structure and layers are coupled by weak van der Waals forces. In the bulk form GeSe is a 1.3 eV indirect band gap semiconductor while it becomes a 1.6 eV direct semiconductor in the monolayer form. Remarkable and unusual optical, mechanical, and electrical properties are anticipated in its monolayer form, however these properties remain unknown to date and are waiting to be discovered. We have tried to mechanically exfoliate the bulk crystal but until now, no single layer could be isolated. To further reduce the thickness of exfoliated GeSe flakes, the laser thinning technique has been applied, using a 473nm CW laser. Following the laser thinning process 10nm thickness GeSe nanosheets were obtained,. This is presented in Figure 5.1 showing a representative section of a thinned GeSe flake obtained via AFM imaging.

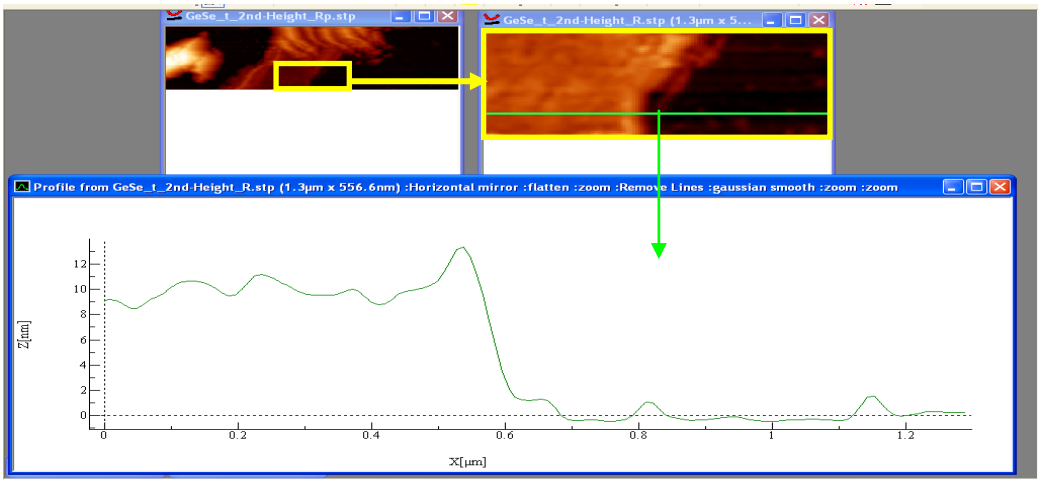

Fig. 5.1: AFM measurement of the laser thinned GeSe nanosheet.

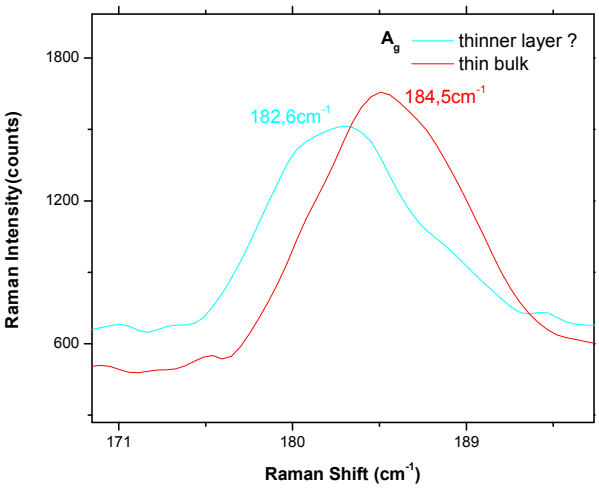

Figure 5.2: Red shift of A_g mode with decreasing thickness.

In a first step, Raman spectroscopy of the pristine and thinned GeSe crystal was performed using the 780nm laser line of the Raman spectrometer, showing two prominent vibrational modes, A_g and B_{2u}. Preliminary experiments shown in Fig 5.2 indicated that the A_g mode appears to red shift with decreasing flake thickness.

Another interesting feature of bulk GeSe is that both prominent vibrational modes become red shifted upon increasing the Raman laser intensity (Fig. 5.3). This is possibly attributed to laser induced heating of the GeSe lattice that "softens" the vibration frequencies.

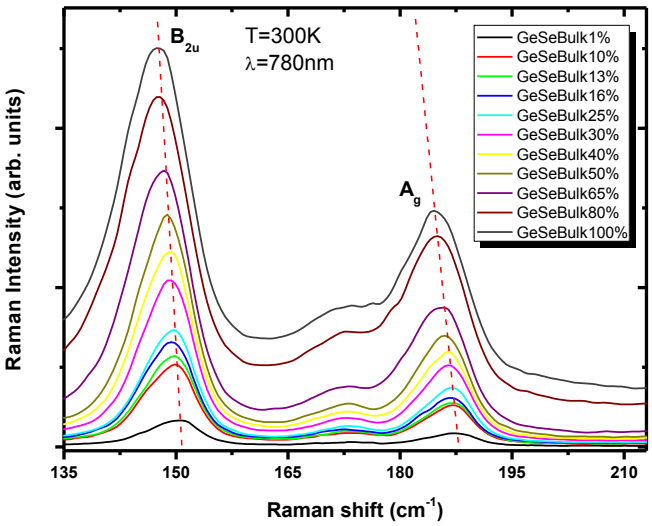

Fig. 5.3: Red shift of both A_g and B_{2u} vibrational modes with increasing laser intensity.

In a second step, we identified the optical damage threshold for the bulk GeSe to be at 350kW/cm^2 (50% of the intensity of the 780nm Raman laser). For laser intensities, below this value, no shift of the Raman modes was observed upon increasing the exposure time. On the contrary, an interesting blue-shift of the Raman modes was observed upon increasing exposure time, for laser intensity values above this threshold (Fig, 5.4). This phenomenon needs explanation and further investigation.

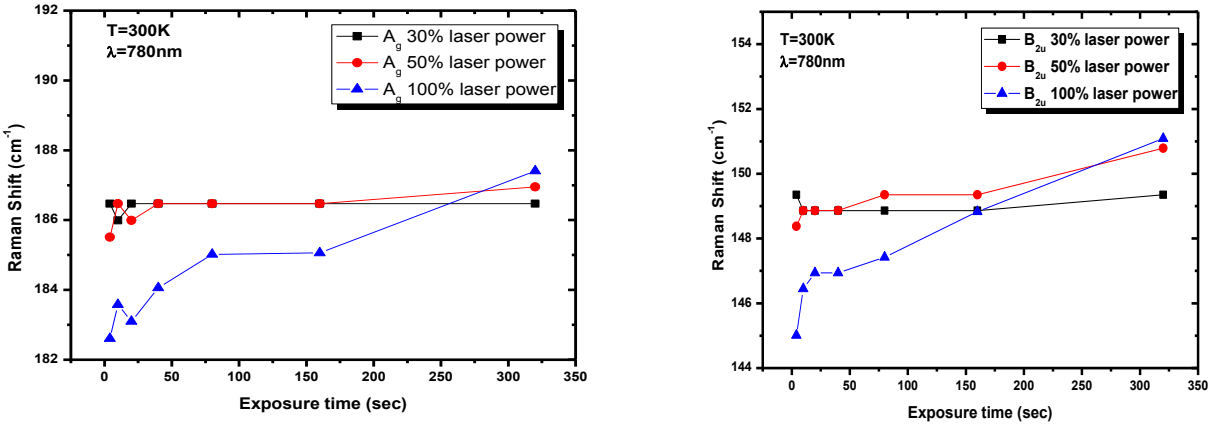

Fig. 5.4: Blue shift of the two prominent vibrational modes with increasing exposure time for bulk GeSe, at excitation laser intensities above the optical damage threshold.

Future studies will include the study of the interaction of ultrashort laser pulses with GeSe crystal, as well as experimental and theoretical analysis of its electronic structure and respective optical properties.

Summary

The first part of this thesis introduced the several MoS_2 production methods. The two possible polytypes of MoS_2 were presented, giving emphasis to the 2H structure that is the most stable and the one that was used in our experiments. Calculations of the electronic structure obtained using the 1st Brillouin zone were shown and the change of the gap from indirect in its bulk form, to direct at the monolayer limit was presented. Absorption and photoluminescence spectra acquired from different research teams, were used to explain the excitonic transitions. In the end of the first chapter, the mechanical properties of Molybdenum disulfide were briefly presented.

In the second chapter, a simple theoretical background of TPA is introduced. In particular, the relation of TPA with the polarization and the third order susceptibility is discussed. Also, the equations of the cross section of OPA and TPA are presented and explained. The optical damage is strongly related with the TPA, when matter interacts with fs pulses of intensity in the range of 10^{12} to 10^{16} W/cm^2. Chapter 2.2 introduces the theory of Raman spectroscopy and presents the mathematical expression of the three types of scattering processes that are involved in a Raman experiment; Rayleigh, Stokes and anti-Stokes. In this thesis, only the Stokes scattering process was used to study the interaction of the ultrafast radiation with the MoS_2 lattice. It subsequently focused on MoS_2 theoretical calculations of phonon dispersion and showed extensively the four main Raman active modes. It is concluded that A_{1g} and E^1_{2g} frequencies are strongly related to the MoS_2 thickness, making Raman spectroscopy a useful technique to indicate the number of layers.

In chapter 3, the methods and the instrumentation used for the experimental part of this thesis are presented. Nicolet Almega XR Micro Raman analysis system and a Light Conversion Pharos fs laser system, were the main apparatuses used.

Chapter 4 contains the experimental results and their interpretation. The effect of intense fs laser excitation on the structure of bulk and monolayer MoS_2 was investigated. The evolution of A_{1g} and E^1_{2g} vibrational modes was recorded as a function of irradiation intensity and total

exposure time. The observed behavior of the Raman peaks were attributed to a corresponding decrease in the number of Mo-S bonds, possibly due to laser-induced bond breaking and subsequent atoms removal. The lack of MoO_3 in the Raman spectra, proposes that the damage of nanosheets occurs through lattice sublimation. The single-pulse optical damage threshold was determined for the monolayer and bulk, under 800 nm wavelength irradiation. The more than 3 times higher damage threshold for the monolayer is understood as the result of a two-photon absorption process versus single-photon absorption in the bulk. This mechanism was verified under a higher wavelength (1030 nm) irradiation where two-photon absorption is required not only for the single layer but also for the bulk. These results may contribute towards the use of MoS_2 as the main material on several applications including mode-lock devices, laser protection optical limiters, saturable absorbers, and optical switches.

In the final and third part of this work, future work and perspectives are presented. The dependence of the laser induced lattice degradation process on pulse duration needs further investigation in order to understand the photothermal and photochemical contributions. Another very important field of future study is the deeper understanding of the physical mechanism behing the ripple-like structures formation on damaged MoS_2 surfaces. Finally, a highly challenging future work is the detailed investigation of the Germanium Selenide 2D crystal. Raman experiments have been performed and present very interesting preliminary data that need further investigation. It is concluded that the study of the interaction of ultrashort laser pulses with the GeSe crystal complemented with micro Photoluminescence and pump-probe experiments, as well as with theoretical calculations of its electronic structure is of great research interest.

The experimental results of this thesis were published in Applied Physics Letters in 29 July 2014, I. Paradisanos, E. Kymakis, C. Fotakis, G. Kioseoglou, E. Stratakis, Appl. Phys. Lett. 105, 041108 (2014).

APPLIED PHYSICS LETTERS **105**, 041108 (2014)

Intense femtosecond photoexcitation of bulk and monolayer MoS_2

I. Paradisanos,[1,2] E. Kymakis,[3] C. Fotakis,[1,2] G. Kioseoglou,[4] and E. Stratakis[1,4,a)]
[1]*Institute of Electronic Structure and Laser (IESL), Foundation for Research and Technology-Hellas (FORTH), Heraklion 71003, Greece*
[2]*Physics Department, University of Crete, Heraklion 71003, Greece*
[3]*Center of Materials Technology and Photonics and Electrical Engineering Department, Technological Educational Institute (TEI) of Crete, Heraklion 71003, Greece*
[4]*Materials Science and Technology Department, University of Crete, Heraklion 71003, Greece*

(Received 22 May 2014; accepted 18 July 2014; published online 29 July 2014)

The effect of femtosecond laser irradiation on bulk and single-layer MoS_2 on silicon oxide is studied. Optical, field emission scanning electron microscopy and Raman microscopy were used to quantify the damage. The intensity of A_{1g} and $E_{2g}{}^1$ vibrational modes was recorded as a function of the number of irradiation pulses. The observed behavior was attributed to laser-induced bond breaking and subsequent atoms removal due to electronic excitations. The single-pulse optical damage threshold was determined for the monolayer and bulk under 800 nm and 1030 nm pulsed laser irradiation, and the role of two-photon versus one photon absorption effects is discussed.
 [http://dx.doi.org/10.1063/1.4891679]

Atomically thin two-dimensional (2D) materials including graphene have attracted significant research interest due to their extraordinary physical properties.[1,2] However, graphene is a zero band gap material which in some cases is an undesirable property for optoelectronic applications.[3] Transition metal dichalcogenides (TMDs) combine the 2D interaction is that the photon energy is transferred to the lattice at rates faster than the electron-phonon relaxation time. Such ultrafast absorption process could give rise to both thermal and non-thermal effects within the lattice. In addition to this, the study of the monolayer response compared to that of the bulk is of great interest, considering the fundamental differen-

REFERENCES

[1] A. H. Castro Neto, F. Guinea, N. M. R. Peres, K. S. Novoselov, and A. K. Geim, Rev. Mod. Phys. 81, 109 (2009).

[2] K. F. Mak, C. Lee, J. Hone, J. Shan, and T. F. Heinz, Phys. Rev. Lett. 105, 136805 (2010).

[3] F. Bonaccorso, Z. Sun, T. Hasan, and A. C. Ferrari, Nat. Photonics 4, 611 (2010).

[4] M. Chhowalla, H. S. Shin, G. Eda, L.-J. Li, K. P. Loh, and H. Zhang, Nat. Chem. 5, 263 (2013).

[5] A. Splendiani, L. Sun, Y. Zhang, T. Li, J. Kim, C.-Y. Chim, G. Galli, and F. Wang, Nano Lett. 10, 1271 (2010).

[6] T. Korn, S. Heydrich, M. Hirmer, J. Schmutzler, and C. Schuller, Appl. Phys. Lett. 99, 102109 (2011).

[7] G. Kioseoglou, A. T. Hanbicki, M. Currie, A. L. Friedman, D. Gunlycke, and B. T. Jonker, Appl. Phys. Lett. 101, 221907 (2012).

[8] Q. H. Wang, K. Kalantar-Zadeh, A. Kis, J. N. Coleman, and M. S. Strano, Nat. Nanotechnol. 7, 699 (2012).

[9] W. Choi, M. Y. Cho, A. Konar, J. H. Lee, G-B. Cha, S. C. Hong, S. Kim, J. Kim, D. Jena, J. Joo, and S. Kim, Adv. Mater. 24, 5832 (2012).

[10] O. Lopez-Sanchez, D. Lembke, M. Kayci, A. Radenovic, and A. Kis, Nat. Nanotechnol. 8, 497 (2013).

[11] R. S. Sundaram, M. Engel, A. Lombardo, R. Krupke, A. C. Ferrari, Ph. Avouris, and M. Steiner, Nano Lett. 13, 1416, (2013).

[12] J. Feng, X. Qian, W. C. Huang, and J. Li, Nat. Photonics 6, 866 (2012).

[13] M. Bernardi, M. Palummo, and J. C. Grossman, Nano Lett. 13, 3664 (2013).

[14] K. Wang, J. Wang, J. Fan, M. Lotya, A. O'Neill, D. Fox, Y. Feng, X. Zhang, B. Jiang, Q. Zhao, H. Zhang, J. N. Coleman, L. Zhang, and W. J. Blau, ACS Nano 7, 9260 (2013).

[15] A. Castellanos-Gomez, M. Barkelid, A. M. Goossens, V. E. Calado, H. S. J. van der Zant, and G. A. Steele, Nano Lett. 12, 3187 (2012).

[16] "Metathetical Precursor Route to Molybdenum Disulfide" Inorganic Syntheses, 1995, vol. 30, 33-37. doi:10.1002/9780470132616.ch8

[17] K. S. Novoselov, D. Jiang, F. Schedin, T. J. Booth, V. V. Khotkevich, S. V. Morozov, and A. K. Geim. Two-dimensional atomic crystals. P. Natl. Aacd. Sci. USA, 102:10451, 2005.

[18] Joensen P, Frindt RF, Morrison SR:Single-layer MoS_2. Mater Res Bull 1986, 21: 457–461.

[19] Miremadi BK, Cowan T, Morrison SR: New structures from exfoliated MoS_2. J Appl Phys 1991, 69: 6373 –6379.

[20] Rao CNR, Nag A: Inorganic analogues of graphene. Eur J Inorg Chem 2010, 2010: 4244 – 4250.

[21] X. Li, W. Cai, J. An, S. Kim, J. Nah, D. Yang, R. Piner, A.Velamakanni, I. Jung, E. Tutuc, S. K. Banerjee, L. Colombo, R. S. Ruoff, Science 2009, 324, 1312-1314.

[22] Y.H. Lee, X.Q. Zhang, W. Zhang, M.T. Chang, C.T. Lin, K.D. Chang, Y.C. Yu, J. T.W. Wang, C.S. Chang, L.J. Li, T.W. Lin, Advanced Materials Volume 24, Issue 17, pages 2320–2325, May 2, 2012.

[23] Y. J. Zhan, Z. Liu, S. Najmaei, P. M. Ajayan and J. Lou, Small, 2012, 8, 966–971.

[24] Y. Lee, J. Lee, H. Bark, I. K. Oh, G. H. Ryu, Z. Lee, H. Kim, J. H. Cho, J.H. Ahn, C. Lee, Nanoscale, 2014, 6, 2821.

[25] A. Castellanos-Gomez, M. Barkelid, A. M. Goossens, V. E. Calado, H. S. J. van der Zant, G. A. Steele, Nano Lett. 2012, 12, 3187−3192.

[26] T. Cao, G. Wang, W. Han, H. Ye, C. Zhu, J. Shi, Q. Niu, P. Tan, E. Wang, B. Liu, J. Feng, Nature Communications, 10.1038/ncomms1882.

[27] J.A. Stewart, D.E. Spearot, Modelling Simul. Mater. Sci. Eng. 21 (2013) 045003

[28] R. Suzuki, M. Sakano, Y. J. Zhang, R. Akashi, D. Morikawa, A. Harasawa, K. Yaji, K. Kuroda, K. Miyamoto, T. Okuda, K. Ishizaka, R. Arita & Y. Iwasa, Nature Nanotechnology 9, 611–617 (2014).

[29] A. N. Enyashin, L. Yadgarov, L. Houben, I. Popov, M. Weidenbach, R. Tenne, M. Bar-Sadan and G. Seifert, J. Phys. Chem. C, 2011, 115, 24586–24591.

[30] Z. M. Wang (ed.), MoS_2, Lecture Notes in Nanoscale Science and Technology, 21

[31] X. Huang, Z. Zeng, H. Zhang, Chem. Soc. Rev., 2013, 42, 1934.

[32] Kuc, A., Zibouche, N., Heine, T.: Influence of quantum confinement on the electronic structure of the transition metal sulfide TS_2. Phys. Rev. B 83, 245213 (2011).

[33] Liao, P.L., Carter, E.A.: New concepts and modeling strategies to design and evaluate photo-electro-catalysts based on transition metal oxides. Chem. Soc. Rev. 42, 2401–2422 (2013).

[34] Jiang, H.: Electronic band structures of molybdenum and tungsten dichalcogenides by the GW approach. J. Phys. Chem. C 116, 7664–7671 (2012).

[35] Ping, Y., Rocca, D., Galli, G.: Electronic excitations in light absorbers for photoelectrochemical energy conversion: first principles calculations based on many body perturbation theory. Chem. Soc. Rev. 42, 2437–2469 (2013).

[36] Matte, H.S.S., Gomathi, A., Manna, A.K., Late, D.J., Dutta, R., Pati, S.K., Rao, C.N.R.: MoS2 and WS2 Analogues of Graphene. Angew. Chem. Int. Ed. 49, 4059–4062 (2010).

[37] He, J., Wu, K., Sa, R., Li, Q., Wei, Y.: Magnetic properties of nonmetal atoms absorbed MoS_2 monolayers. Appl. Phys. Lett. 96, 082504 (2010).

[38] Enyashin, A., Gemming, S., Seifert, G.: Nanosized allotropes of molybdenum disulfide. Eur. Phys. J. 149, 103–125 (2007).

[39] Botello-Mendez, A.R., Lopez-Urias, F., Terrones, M., Terrones, H.: Metallic and ferromagnetic edges in molybdenum disulfide nanoribbons. Nanotechnology 20, 325703 (2009).

[40] Kumar, A., Ahluwalia, P.K.: Electronic structure of transition metal dichalcogenides monolayers 1H-MX_2 (M = Mo, W; X = S, Se, Te) from ab initio theory: new direct band gap semiconductors. Eur. Phys. J. B 85, 186 (2012).

[41] Kadantsev, E.S., Hawrylak, P.: Electronic structure of a single MoS_2 monolayer. Solid State Commun. 152, 909–913 (2012).

[42] Ding, Y., Wang, Y.L., Ni, J., Shi, L., Shi, S.Q., Tang, W.H.: First principles study of structural, vibrational and electronic properties of graphene-like MX_2 (M = Mo, Nb, W, Ta; X = S, Se, Te) monolayers. Physica B 406, 2254–2260 (2011).

[43] Cheiwchanchamnangij, T., Lambrecht, W.R.L.: Quasiparticle band structure calculation of

monolayer, bilayer, and bulk MoS2. Phys. Rev. B 85, 205302 (2012).

[44] Komsa HP, Krasheninnikov AV (2012) Effects of confinement and environment on the electronic structure and exciton binding energy of MoS_2 from first principles. Phys. Rev. B 86, 241201(R)

[45] Johari, P., Shenoy, V.B.: Tuning the electronic properties of semiconducting transition metal dichalcogenides by applying mechanical strains. ACS Nano 6, 5449–5456 (2012)

[46] Yue, Q., Kang, J., Shao, Z.Z., Zhang, X.A., Chang, S.L., Wang, G., Qin, S.Q., Li, J.B.: Mechanical and electronic properties of monolayer MoS_2 under elastic strain. Phys. Lett. A 376, 1166–1170 (2012).

[47] A. Splendiani, L. Sun, Y. B. Zhang, T. S. Li, J. Kim, C. Y. Chim, G. Galli and F. Wang, Nano Lett., 2010, 10, 1271–1275.

[48] Feng, W.X., Yao, Y.G., Zhu, W.G., Zhou, J.J., Yao, W., Xiao, D.: Intrinsic spin Hall effect in monolayers of group-VI dichalcogenides: A first-principles study. Phys. Rev. B 86, 165108 (2012).

[49] Li, X., Zhang, F., Niu, Q.: Unconventional quantum hall effect and tunable spin hall effect in dirac materials: application to an isolated MoS2 trilayer. Phys. Rev. Lett. 110, 066803 (2013).

[50] M. M. Benameur, B. Radisavljevic, J. S. He´ron, S. Sahoo, H. Berger and A. Kis, Nanotechnology, 2011, 22, 125706.

[51] A. Castellanos-Gomez, M. Poot, G. A. Steele, H. S. J. van der Zant, N. Agrait and G. Rubio-Bollinger, Adv. Mater., 2012, 24, 772–775.

[52] S. Bertolazzi, J. Brivio and A. Kis, ACS Nano, 2011, 5, 9703–9709.

[53] Robert W. Boyd, Nonlinear Optics, 3rd Edition, 2008

[54] M. Cardona. Light Scattering in Solids II, Springer, Berlin, 1982.

[55] A. Molina-Sánchez and L. Wirtz, Phys. Rev. B 84, 155413

[56] N. Wakabayashi, H. G. Smith, and R. M. Nicklow. Phys. Rev. B 12, 659 (1975)

[57] C.V. Ramana, U. Becker, V. Shutthanandan , C.M. Juliev, Geochemical Transactions 2008,9:8

[58] C. Lee, H. Yan, L. E. Brus , T. F. Heinz, J. Hone, S. Ryu, ACS Nano, 2010, 4 (5)

[59] T. Li, G. Galli, J. Phys. Chem. C 2007, 111, 16192–16196.

[60] B. J. Mrstik, R. Kaplan, T. L. Reinecke, M. V. Hove, Tong, Phys. Rev. B 1977, 15, 897–900.

[61] D. Yang, S. J. Sandoval, W. M. R. Divigalpitiya, J. C. Irwin, R. F. Frindt, Phys. Rev. B 1991, 43, 12053–12056.

[62] P. Bertrand, Phys. Rev. B 1991, 44, 5745–5749.

[63] Y. Y. W. Z. H. Ni, Z. X. Shena, H. M. Wang, Y. H. Wu, Appl. Phys. Lett. 2008, 92, 043121/1–043121/3.

[64] H. Zeng, J. Dai, W. Yao, D. Xiao, and X. Cui, Nat. Nanotechnol. 7, 490 (2012).

[65] M. Currie, J. D. Caldwell, F. J. Bezares, J. Robinson, T. Anderson, H. Chun, M. Tadjer, Appl. Phys. Lett. 99, 211209 (2011).

[66] A. Roberts, D. Cormode, C. Reynolds, T. Newhouse-IIIige, B. J. LeRoy, A. S. Sandhu, Appl. Phys. Lett. 99, 051912 (2011).

[67] R. Zan, Q. M. Ramasse, R. Jalil, T. Georgiou, U. Bangert, and K. S. Novoselov, ACS Nano 7, 10167 (2013).

[68] B. C. Windom, W. G. Sawyer, and D. W. Hahn, Tribol. Lett. 42, 301 (2011).

[69] L. Jensen, M. Mende, S. Schrameyer, M. Jupe, and D. Ristau, Opt. Lett. 37, 4329 (2012).

[70] N. Bloembergen, IEEE J. Quantum Electron. 10, 375–386 (1974).

[71] G. D. Tsibidis, M. Barberoglou, P. A. Loukakos, E. Stratakis, and C. Fotakis, Phys. Rev. B 86, 115316 (2012).